EXPERIMENTAL INVESTIGATION ON THE EFFECT OF PERMEABILITY ON THE OPTIMUM ACID FLUX IN CARBONATE MATRIX ACIDIZING

A Thesis

by

JORDAN RUBY ETTEN

Submitted to the Office of Graduate and Professional Studies of
Texas A&M University
in partial fulfillment of the requirements for the degree of

MASTER OF SCIENCE

Chair of Committee,	Ding Zhu
Co-Chair of Committee,	A. Daniel Hill
Committee Member,	Yuefeng Sun
Head of Department,	A. Daniel Hill

May 2015

Major Subject: Petroleum Engineering

ABSTRACT

Determination of optimal acidizing conditions through laboratory experimental study is crucial for designing matrix acid stimulation jobs in the field. Optimum interstitial velocity, $v_{i\text{-}opt}$ (the velocity of injected fluid that yields the minimum volume of acid needed to propagate wormholes) can be determined though curve fitting of experimental data. This optimum interstitial velocity coincides with the minimum volume of acid required for wormhole breakthrough, and therefore, the most efficient stimulation design. Optimum interstitial velocity determines the injection rate for a treatment, and the optimum pore volume to breakthrough, $PV_{bt\text{-}opt}$, suggests the total volume of acid needed. Studies of carbonate matrix acidizing have focused on the role of many parameters, such as acid concentration, acid type, temperature, and core dimensions. However, under the same experimental conditions, different limestone rocks exhibit different optimal conditions. It is important to explore how changes in rock properties, such as permeability and pore structure, can also impact the efficacy of matrix acidizing techniques.

In this work, a series of linear coreflood experiments on relatively homogenous Indiana limestone and Desert Pink limestone cores were performed at ambient temperature. Cores of 1.5-in. diameter by 8-in. long were acidized using 15% hydrochloric acid. The average permeabilities of the cores tested were 6, 11, 33 and 239 mD with varied porosity. The effects of permeability and porosity were isolated using thin section analysis to study pore structure. Based on experimental results, a

detailed explanation of the pore structure and permeability effects on optimum interstitial velocity is presented.

The coreflood acidizing results show that at low permeabilities, optimum interstitial velocity increases with permeability. When permeability of the rock reaches a certain value, the effect of permeability on the optimum injection condition diminishes. In addition, the optimum pore volume to breakthrough increases across the entire range of permeabilities tested. This work also briefly quantifies the differences in pore structure of the samples, leading to recommendations for future work. The implications and applications of this work are far-reaching; better understanding of optimal acidizing conditions based on the studied rock properties has significant potential economic and operational impact.

DEDICATION

This thesis is dedicated to my parents.

To my Dad- I never would've thought that I'd want to do the same thing as you but that plan completely failed! Thanks for being a great role model, for introducing me to the oil industry, for giving me wings instead of roots and for all the love and encouragement along the way.

To my Mom- Thanks for being my biggest supporter through thick and thin, your endless encouragement, and your unconditional love.

ACKNOWLEDGEMENTS

I would like to thank my committee chair, Dr. Zhu, and my committee members, Dr. Hill, and Dr. Sun, for their guidance and support throughout the course of this research.

Thanks to my friends, colleagues and the department faculty and staff for making my time at Texas A&M University a great experience. Thanks especially to Kai Dong, Haoran Cheng and Jimmy Jin for all the help with running experiments. I also want to extend my gratitude to the Acid Stimulation Research Program (ASRP), for their financial support of this project.

Most importantly, thanks to my family and friends for all your love and support. Thanks to my parents, John and Kathy, for always encouraging me to follow my dreams. Thanks to Murphy and Rizzo for keeping me company for hundreds of hours as I worked. Thanks to my sister, Kallie, for being my best friend and always being there when needed.

NOMENCLATURE

A	Cross sectional area of core, cm^2
$c_{experimental}$	Concentration of acid used in experiments, weight percent
c_{stock}	Concentration of stock acid, weight percent
d	Core diameter, cm
ID	Internal diameter of tubing, in
J	Sum of squared residuals, dimensionless
J_D	Productivity index, dimensionless
k	Permeability, mD
L	Core length, cm
L_{tubing}	Length of tubing between acid accumulator and core inlet, cm
M_{dry}	Mass of dry core, g
$M_{saturated}$	Mass of saturated core, g
PV_{bt}	Pore volume breakthrough, dimensionless
$PV_{bt\text{-}opt}$	Optimum pore volume breakthrough, dimensionless
p	Pressure, psi
p_{wf}	Bottomhole flowing pressure, psi
q	Injection flow rate, cm^3/min
r_e	Wellbore drainage radius, ft
r_w	Wellbore radius, ft
s	Skin factor, dimensionless

t	Injection time, sec
t_0	Time acid injection begins, sec
t_1	Time for acid to reach core, sec
t_2	Wormhole breakthrough time, sec
V_{acid}	Volume of acid required for wormhole breakthrough, cm^3
V_{bulk}	Bulk volume of core, cm^3
$V_{experimental}$	Volume of acid at desired concentration, mL
V_{pore}	Pore volume, cm^3
V_{stock}	Volume of stock acid, mL
V_{tubing}	Volume of pipe between acid accumulator and core inlet, cm^3
V_{water}	Volume of water, mL
v_i	Interstitial velocity, cm/min
$v_{i\text{-}opt}$	Optimum interstitial velocity, cm/min
W_B	Wormhole B factor constant in Buijse-Glasbergen model, $(m/s)^{-2}$
W_{eff}	Wormhole efficiency constant in Buijse-Glasbergen model, $(m/s)^{1/3}$
$\emptyset$	Porosity, fraction
μ	Viscosity, cp
ρ_{brine}	Density of brine, g/cm^3
$\rho_{experimental}$	Density of acid at concentration used in experiments, g/cm^3
ρ_{stock}	Density of stock acid, g/cm^3

TABLE OF CONTENTS

Page

ABSTRACT ii

DEDICATION iv

ACKNOWLEDGEMENTS v

NOMENCLATURE vi

TABLE OF CONTENTS viii

LIST OF FIGURES x

LIST OF TABLES xiii

1. INTRODUCTION 1

1.1 Background 1
1.2 Literature Review 4
1.3 Problem Statement 15
1.4 Research Objectives 18

2. EXPERIMENTAL APPARATUS 19

2.1 Experimental Apparatus Overview 19
2.2 Syringe Pump 20
2.3 Accumulation System 21
2.4 Core Holder 23
2.5 Hydraulic Hand Pump 25
2.6 Backpressure Regulation 26
2.7 Data Acquisition System 28

3. EXPERIMENTAL PROCEDURE 30

3.1 Experimental Summary 30
3.2 Cores 31

3.3 Data Recording....33
3.4 Core Preparation....34
3.5 Porosity Measurement....36
3.6 Acid Preparation....36
3.7 Accumulation System Setup....37
3.8 Core Holder Setup....41
3.9 Pressure Build Up and Permeability Test....43
3.10 Acidizing Procedure....47
3.11 Depressurizing and Cleaning System....49
3.12 Pressure Analysis....50
3.13 Thin Section Analysis....51

4. RESULTS AND DISCUSSION....52

4.1 Determining Pore Volume Breakthrough....52
4.2 Determining Optimum Interstitial Velocity....55
4.3 Effect of Permeability on Optimal Conditions....59
4.4 Pore Structure Effect....64

5. CONCLUSION AND RECOMMENDATIONS....74

REFERENCES....76

APPENDIX A....80

APPENDIX B....82

APPENDIX C....85

LIST OF FIGURES

Page

Figure 1.1 - Post-acidization skin values obtained from buildup test data (Furui et al., 2012). 3

Figure 1.2 - Dissolution patterns observed at different injection rates in carbonates (McDuff et al., 2010). 6

Figure 1.3- Wormhole efficiency relationships generated by experimental data and curve fitted with the Buijse and Glasbergen model (Buijse and Glasbergen, 2005). 8

Figure 1.5- Data fit for Fredd and Fogler (1999) (Talbot and Gdanski, 2008). 12

Figure 1.6 - Data fit for Bazin (2001) (Talbot and Gdanski, 2008). 12

Figure 1.7- 3-D wormhole structures at optimum injection rate (McDuff et al., 2010)...14

Figure 1.8- Master wormhole efficiency curve for different carbonate rock types based on their flowing fraction (Zakaria et al., 2015). 17

Figure 2.1 – Coreflood system schematic (Dong, 2012).....19

Figure 2.2- Teledyne ISCO syringe pump (Grabski, 2012). 21

Figure 2.4- Core holder (Dong, 2012).....23

Figure 2.5- Core holder caps. 25

Figure 2.6 - Hydraulic hand pump (Enerpac, 2015).....26

Figure 2.7- Equilibar backpressure regulator (Equilibar, 2015). 26

Figure 2.8 - Internal structure of a backpressure regulator (Equilibar, 2015). 28

Figure 2.9- Foxboro pressure transducer. 29

Figure 3.1- Core saturation equipment: (a) glass bell container, (b) PVC container, (c) vacuum pump. 35

Figure 3.2- Schematic of accumulation system. 38

Figure 3.3- Core holder connections schematic. 42

Figure 3.4- Hydraulic hand pump valves (Enerpac, 2015). 43

Figure 3.5- Typical pressure buildup curve due to water injection. 46

Figure 3.6- Schematic of injection valves. 48

Figure 3.7 - Schematic of pressurized system. 50

Figure 4.1- Typical acidization pressure curve with critical times. 54

Figure 4.2- Desert Pink experimental data. 57

Figure 4.3- Using Excel Solver to solve for optimal conditions. 59

Figure 4.4- Experimental results of wormhole efficiency with different permeabilities. 60

Figure 4.5- Buijse-Glasbergen curve fitted results for different permeabilities. 61

Figure 4.6- Effect of permeability on optimal pore volumes to breakthrough. 63

Figure 4.7- Thin section images for each permeability group. 65

Figure 4.8- Comparison of (a) Austin chalk (Ziauddin and Bize, 2007) and (b) Desert Pink limestone. 67

Figure 4.9- Post-acidization CT images of cores from different rock groups. 68

Figure 4.10- Pore throat-size distribution for (a) Indiana limestone and (b) Desert Pink limestone (Zakaria et al., 2015). 70

Figure 4.11- Buijse-Glasbergen curve fitted results for Indiana limestone samples of different permeabilities. 73

Figure C.1- CT scans of 11 mD Indiana limestone (cores 4, 3 & 2). 86

Figure C.2- CT scans of 11 mD Indiana limestone (cores 1, 5 & 6). 87

Figure C.3- CT scans of 33 mD Desert Pink limestone (cores 6, 9 & 5). 88

Figure C.4- CT scans of 33 mD Desert Pink limestone (cores 3, 1, 4 & 8). 89

Figure C.5- CT scans of 239 mD Indiana limestone (cores 6, 5 & 4). 90

Figure C.6- CT scans of 239 mD Indiana limestone (cores 1, 3 & 2).....91

LIST OF TABLES

Page

Table 3.1 - Summary of core properties. 32

Table 3.2- Average pore properties of each set of experiments. 33

Table 3.3- Sample matrix acidizing data worksheet. 33

Table 3.4- HCl acid volumes for dilution 37

Table 4.1- Desert Pink (33 mD) experimental data 56

Table 4.2- Summary of optimal conditions. 62

Table 4.3- Flowing fractions for Indiana limestone and Desert Pink limestone (Zakaria et al., 2015). 71

Table A.1- Indiana limestone (6 mD) experimental data. 80

Table A.2- Indiana limestone (11 mD) experimental data. 80

Table A.3- Indiana limestone (239 mD) experimental data. 81

Table B.1- Conversion factors for Darcy's Law. 83

1. INTRODUCTION

1.1 Background

The condition of the near-wellbore region greatly impacts well productivity. Reservoir radial fluid flow to the wellbore results in high flow velocities, which creates a large near wellbore pressure drop. When the permeability or flow path change in the near wellbore region, a significant additional pressure drop results. This additional pressure drop is known as the skin effect. This skin effect can be either negative or positive and is added to the pressure drop across the reservoir as shown in Eq. 1.1.

$$p_{re} - p_{wf} = \frac{q\mu}{2\pi kh}\left(\ln\frac{r}{r_w} + s\right) \quad \text{.....(1.1)}$$

A major goal of acid stimulation design is to cost-effectively maximize the productivity index of a well. Eq. 1.2 presents the dimensionless productivity index, J_D, (for steady state conditions).

$$J_D = \frac{1}{\ln\left(\frac{r_e}{r_w}\right)+s} \quad \text{.....(1.2)}$$

Therefore, inducing negative skin or eliminating positive skin should result in a well productivity improvement.

Stimulating wells by acidization or hydraulic fracturing reduces skin effects. In these stimulation techniques, highly permeable paths from the wellbore into the reservoir are created. These paths increase fluid conductivity near wellbore and therefore reduce the pressure drop. The selection of a stimulation technique is based on many factors such as formation properties, production goals and economics.

Matrix acidizing, which involves injecting acid below a formation fracture pressure, is commonly used in carbonate reservoirs. During acidizing of carbonates, long channels called "wormholes" are formed due to high surface reaction rates between carbonates and acid. Hydrochloric acid (HCl) is most commonly used to dissolve the minerals present in carbonate rocks through the following chemical reactions.

For calcite: $CaCO_3 + 2HCl \rightarrow CaCl_2 + CO_2 + H_2O$……...(1.3)

For dolomite: $4HCl + CaMg(CO_3)_2 \rightarrow CaCl_2 + MgCl_2 + 2CO_2 + 2H_2O$……(1.4)

Due to the high surface reaction rates between reactants, mass transfer limits the overall reaction rate in carbonates. As a result, non-uniform dissolution patterns are formed which lead to wormholes. On the other hand, in sandstone formations, wormholes are not created and only damage within pores is removed. In these formations, mud acid (3 wt% hydrofluoric acid and 12 wt% hydrochloric acid) is typically used. Due to the slow surface reaction rate with the formation, uniform dissolution occurs which only removes acid soluble damage in pores near wellbore. As a result, sandstone matrix acidizing can only restore the natural productivity of a well

(skin equal to zero). On the other hand, matrix acidizing can induce negative skin, and therefore enhance productivity, through the creation of wormholes in carbonate reservoirs (Glasbergen et al., 2009 and Economides et al., 2013).

The ultimate goal in carbonate matrix acidizing is to create wormholes long enough to bypass near wellbore damage. These wormholes are capable of propagating tens of feet from the wellbore (Economides et al., 2013). Furui et al. (2012) analyzed approximately 400 wells in Middle Eastern limestone reservoirs and North Sea chalk reservoirs. As seen in **Fig 1.1**, their work discovered an average post acidization skin factor of -4. Therefore, with the correct stimulation design, matrix acidizing can effectively reduce skin and increase well productivity.

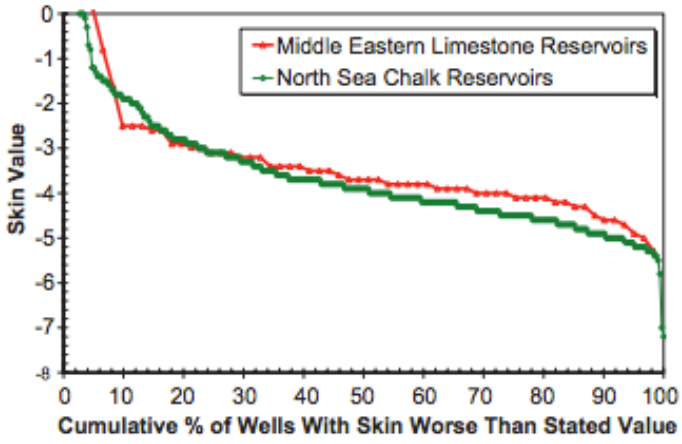

Figure 1.1 - Post-acidization skin values obtained from buildup test data (Furui et al., 2012).

1.2 Literature Review

Many studies have been completed to try and understand wormhole growth mechanisms in carbonate formations. Buijse (1997) explained the two critical processes that must be understood to model wormhole mechanisms. The first process involves acid spending and reaction with the rock pores. This includes convection (which is directly impacted by the acid injection rate), the surface reaction rate and molecular diffusion. Due to the fast reaction rate between hydrochloric acid and carbonates, propagation of wormholes results from a diffusion limited reaction. The second process mentioned by Buijse (1997) involves flow effects including fluid loss and fluid distribution. This directly impacts the geometry of the wormholes. Fluid loss to the formation affects the length of the wormhole while fluid distribution affects the density of wormholes formed.

Several studies have focused on how the acid injection rate affects wormhole growth. Williams et al. (1979) published some of the earliest work on wormholing in which they suggested that acid should be pumped at the highest possible injection rate without fracturing the reservoir rock to obtain the best stimulation results. Daccord (1987) injected water into plaster and observed different wormhole dissolution pattern at different injection rates. Daccord et al. (1989) furthered his research and developed a wormhole propagation model in which wormholes were quantified by their equivalent hydraulic length. This model led to the conclusion that an optimum flow rate exists for highly reactive systems. Furthermore, he suggested that acid injection rates used in the field were too high.

Hoefner and Fogler (1989) conducted similar experiments to Daccord by performing linear coreflooding experiments in which they injected HCl into limestone and dolomite cores. They discovered that with higher injection rates, wormhole propagation efficiency increases. However, at very high flow rates, efficiency is reduced. In addition, they observed that different wormhole dissolution patterns form during acidization. **Fig. 1.2** shows CT images of these different wormhole dissolution patterns (McDuff et al. 2010). At low injection rates, compact dissolution at the core inlet occurs, resulting in an inefficient use of acid. In comparison, at high injection rates, more uniformed, highly branched wormholes are formed. This also results in an inefficient use of acid as fluid is forced into smaller pores, creating several small channels. At immediate injection rates, a single dominant wormhole is formed. These dissolution patterns are discussed in more detail in Fredd and Fogler's (1998) work.

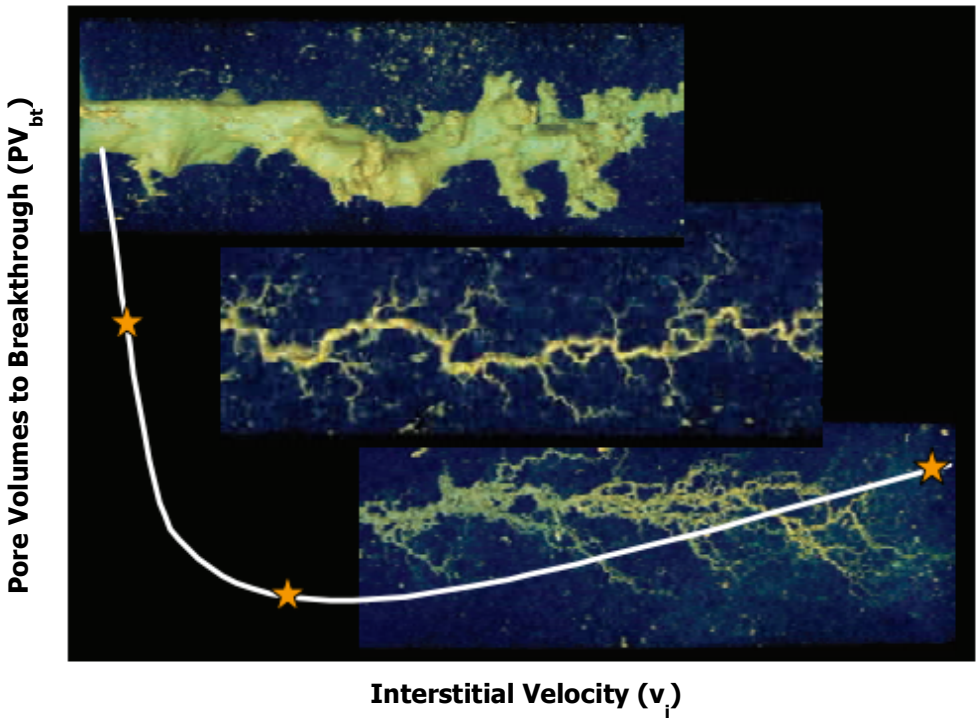

Figure 1.2 - Dissolution patterns observed at different injection rates in carbonates (McDuff et al., 2010).

Wang et al. (1993) conducted coreflood experiments and confirmed that the point at which a single dominant wormhole is formed represents the optimum injection rate. This rate corresponds to the best stimulation results while requiring the minimum volume of acid. It is dependent on both fluid and rock properties. This optimum point has become the focus of many matrix acidizing experimental studies.

Wormhole efficiency relationships illustrate that an optimal condition exists that is critical in developing carbonate matrix acidizing stimulation models. **Fig. 1.3** presents an example of such a relationship (Buijse and Glasbergen, 2005). The curves in Fig. 1.3

are created through coreflood experiments at various acid injection rates. The pore volumes to breakthrough (the amount of acid required to breakthrough the core in terms of pore volumes) is calculated at each injection rate and plotted as a function of the interstitial velocity (the velocity of the injected fluid through the pore space cross sectional area). It is important to note the slope of the curves before and after the optimum point. At injection rates lower than the optimum, the slope of the curve is steep, indicating that the volume of acid necessary decreases greatly with increasing injection rates. On the other hand, the slope beyond the optimum point is more gradual, resulting in only small increases in acid volume at higher injection rates. This indicates that injecting acid at higher rates is preferred to pumping at low rates for a more efficient use of acid (Economides, et al., 2013).

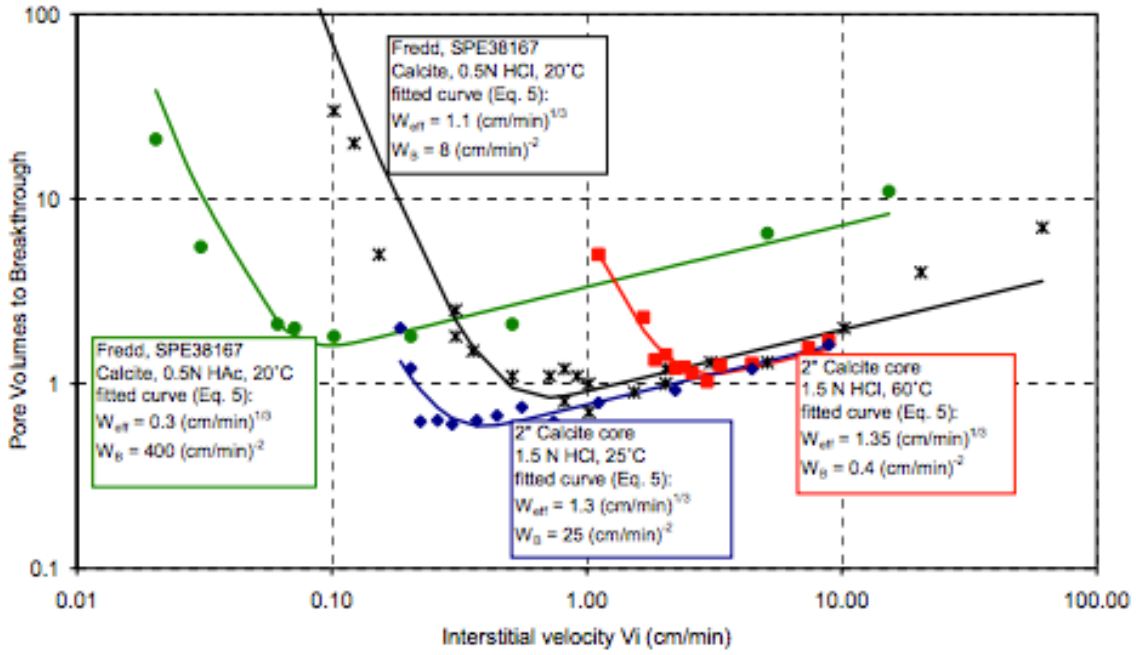

Figure 1.3- Wormhole efficiency relationships generated by experimental data and curve fitted with the Buijse and Glasbergen model (Buijse and Glasbergen, 2005).

Several theoretical models have been developed to try and understand the process of carbonate wormholing. Many models start with the basic chemistry and physics at the microscopic level and then attempt to scale up to field conditions while capturing both the operational and rock parameters. While all these models provide new insight on wormhole growth, no model has fully captured all aspects of wormholing. Fredd and Miller (2000) provide an overview of some of the existing models. They divide existing models into five different approaches: transition pore theories, capillary tube models, Peclet number theories, Damköhler number theories, and network models. Brief explanations of some of the most critical models are summarized as follows.

Wang et al. (1993) presented a transition pore theory for the calculation of optimal acid interstitial velocity through the use of the maximum pore diameter. They stated that dominant wormholes are formed at pores that are greater than the transition pore size. This critical transition pore size is obtained by equating the growth rate functions in large pores (controlled by mass transfer) and small pores (limited by the surface reaction). This method requires knowledge of pore dimensions that are difficult to measure.

Capillary tube models employ convection-diffusion equations for the reaction of acid down bundles of tubes. These equations can be combined with wormhole density estimations to determine the growth rate and volume of acid needed for wormholes. Huang et al. (1999) developed a method to predict the wormhole density, or number of major wormholes formed per area, by modeling the pressure field around a wormhole. Due to the reduced flux caused by the propagation of a wormhole, initiation of other wormholes is repressed. Combining this density approach with a propagation model is crucial in determining acid volumes needed for field operations. However, this model also requires pore parameters that are difficult to quantify.

Hoefner and Fogler (1988) were the first to account for the effect of wormhole structure in their study through a network approach. They studied the dissolution of dolomite and calcite by HCl and determined that the Damköhler number governs wormhole formation. The Damköhler number is a dimensionless value defined as the ratio of the acid reaction rate to the acid convection rate. Different Damköhler numbers result in different wormhole structures. Fredd and Fogler (1999) further studied the

dependence of wormholing on the Damköhler number in a range of fluid systems, including strong acids, weak acids and chelating agents. They determined that the optimum Damköhler number of 0.29 corresponds to the optimal injection rate for different types of fluids and formations. The Damköhler number is important as it accounts for a wide range of transport and surface reactions. Additional studies have utilized the Damköhler number along with other factors to create even more detailed models (Golfier et al., 2001 and Panga et al., 2004).

While the models previously described are successful in predicting wormholing in ideal situations, conditions are often much more complex. Buijse and Glasbergen (2005) created a simple semi-empirical model that accounts for a wider range of parameters. They modeled wormhole growth rate as a function of interstitial velocity. Their model is easy to use as only two parameters (interstitial velocity and the corresponding pore volumes to breakthrough) are required and can be obtained by coreflood experiments. Temperature, permeability, mineralogy and acid concentration are all incorporated within these two experimental values. Furui et al. (2012) concluded that the tip velocity of the dominant propagating wormhole is critical for wormhole growth. The results were incorporated into the Buijse and Glasbergen model to obtain an integrated flow model that accounts for core size dependencies.

Several linear coreflood experiments have been performed to determine the optimal acidizing conditions under different conditions. Wang et al. (1993) studied the effect of temperature and acid concentration. Fredd and Fogler (1998) focused on temperature and three different types of acid (hydrochloric, acetic and

ethylenediaminetetracacetic acid). Bazin (2001) studied the effect of acid concentration, temperature, permeability and core length. Dong et al. (2012) investigated the effects of core dimensions further. Talbot and Gdanski (2008) successfully curve fitted some of this experimental data using the Buijse- Glasbergen model to determine the optimal wormholing conditions (**Fig.1.4**, **Fig 1.5**, and **Fig 1.6**).

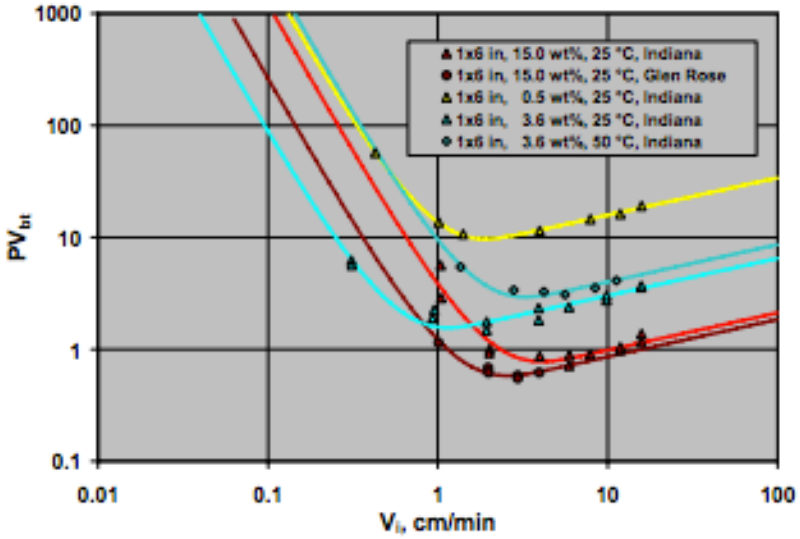

Figure 1.4- Data fit for Wang et al. (1993) (Talbot and Gdanski, 2008).

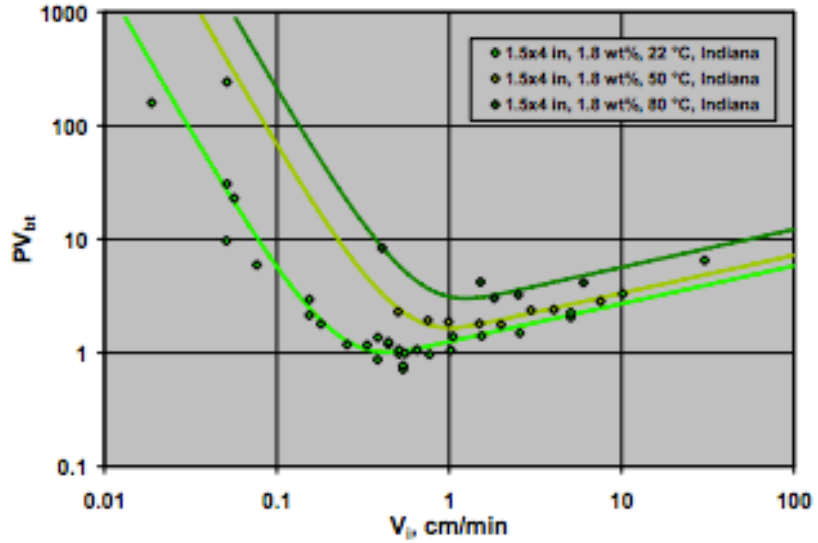

Figure 1.5- Data fit for Fredd and Fogler (1999) (Talbot and Gdanski, 2008).

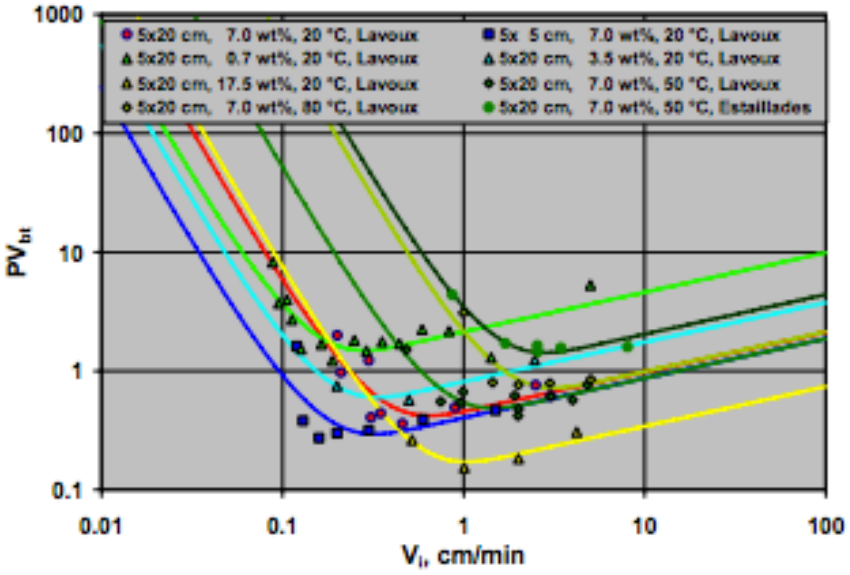

Figure 1.6 - Data fit for Bazin (2001) (Talbot and Gdanski, 2008).

To better understand the flow conditions in the field, radial coreflood experiments have been completed. Frick et al. (1994) performed radial flow corefloods and discovered an optimum condition also exists in radial flow. This optimum velocity is significantly lower than the optimal conditions observed in the field. They also concluded that while radial corefloods are more difficult to perform than linear corefloods, they provide a better indication of field conditions. Mostofizadeh and Economides (1994) also performed radial coreflood experiments and developed a simple method to upscale the lab results to field conditions. Their model involves first calculating the acid capacity number, which is a ratio of the amount of dissolved mineral in the pore space to the amount of mineral present (Economides et al., 2013), and then determining the volume of acid needed for the optimum injection rate. The optimum field injection rate is calculated through a simple volumetric ratio.

Several other radial flow models have been developed as well. Buijse and Glasbergen (2005) compared the differences between linear and radial geometry and determined that interstitial velocity decreases as a function of the distance from the wellbore in radial geometry. This results from fluid loss to the formation over time. In linear geometries, fluid loss is independent of wormhole length. However, in radial geometries, the cross sectional area in front of the propagating wormhole increases with increasing distance from the wellbore. This results in an increase of fluid loss with increasing wormhole length. Therefore, the wormhole growth rate decreases with increasing length. To account for this, Buijse and Glasbergen (2005) presented an integration method for determining the wormhole penetration depth. Based on this value,

the growth rate of the wormhole under radial flow can be calculated and used in their semi-empirical model.

While radial coreflood experiments provide information on wormhole growth mechanisms in 2-D, McDuff et al. (2010) went a step further by performing larger scale experiments to see the 3-D wormhole propagation patterns. In their work, large square rock samples 14 ft^3 in volume were acidized and imaged using a CT scanner. **Fig 1.7** presents the images they obtained. Understanding the characteristics of 3-D wormhole patterns is important when predicting the long-term performance of stimulated formations.

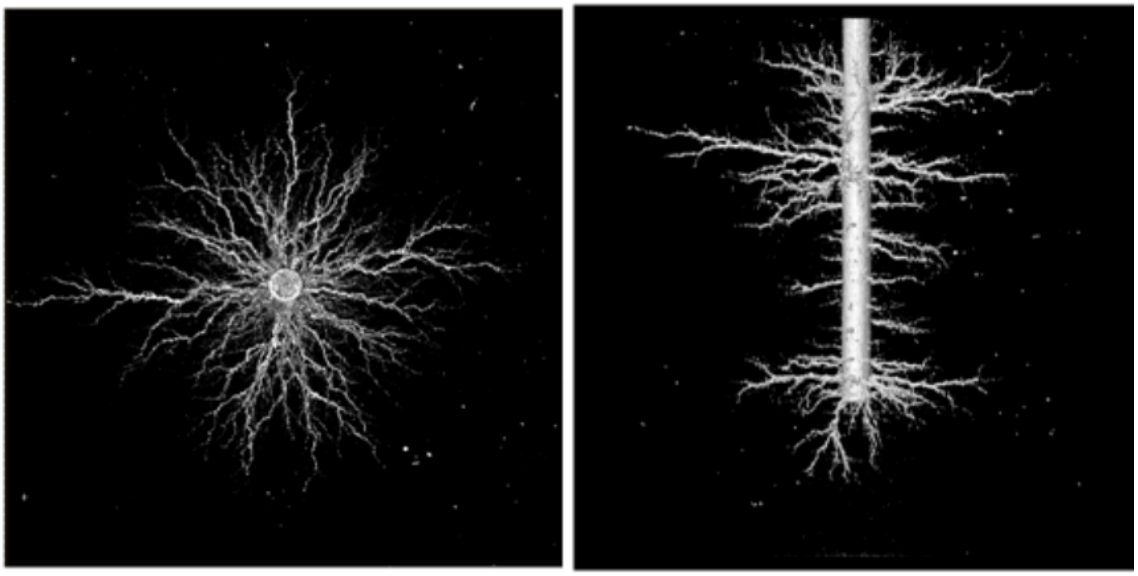

Figure 1.7- 3-D wormhole structures at optimum injection rate (McDuff et al., 2010).

Coreflood experiments have provided valuable information regarding wormhole propagation. However, many other factors play a role in the field. Abou-Sayed et al. (2005) explains some of the other factors that must be considered to effectively stimulate thick carbonate reservoirs. It is important to consider the following: equipment requirements and capabilities, operational risks and costs, heterogeneity in rock type, permeability, injection temperature, and reservoir pressure. In addition, Mazel et al. (2007) stressed the importance of well orientation and wellbore effects (include lag time between pumping and delivery to the formation). While knowledge is expanding regarding matrix acidizing, there is still a need for more accurate models for field conditions.

1.3 Problem Statement

Previous carbonate matrix acidizing research has focused on the role of many parameters, such as acid concentration, acid type, temperature, and core dimensions on the optimum interstitial velocity. However, under the same experimental conditions, different limestone rocks exhibit different optimal conditions due to their varied rock properties.

The effect of permeability on the optimal matrix acidizing conditions has briefly been studied before. Bazin (2001) observed that with increasing permeability, the optimal interstitial velocity and it's corresponding pore volumes to wormhole breakthrough increases. Two sets of core samples were investigated in her work, one with a permeability range of 2.1-9.2 mD and the other with a range of 170 -220 mD.

Frick et al. (1994), and Mostofizadeh and Economides (1994) conducted radial flow coreflood experiments to study the effect of permeability. They discovered that permeability has a qualitatively similar effect as the acid injection rate and predicted that with increasing permeability, the optimum interstitial velocity would also increase. Their results were based on two sets of cores, one had a permeability range of 0.2-0.4 mD and the other had a permeability range of 0.7-1 mD.

Ziauddin and Bize (2007) studied the influence of rock properties, in particular pore scale heterogeneities on matrix acidizing treatments. Based on a study of eight different types of limestones (with permeabilities ranging from 0.2 – 80 mD), they classified the rocks into Reservoir Rock Types (RRT). The classification was based mainly on porosity spatial distribution. Other characterization factors included mineralogy, texture and rock fabric. Experiments completed included Nuclear Magnetic Resonance (NMR), Computed Tomography (CT) scanning, Scanning Electron Microscopy (SEM), resistivity tests, and high-pressure mercury injection. The RRTs were used to generate a few type curves that predict the optimal matrix acidizing conditions for that particular group. Rock samples with similar porosity spatial distribution exhibited similar trends in pore volumes to breakthrough values.

Zakaria et al. (2015) recently published a study in which they quantified carbonate pore scale heterogeneity resulting from pore size, shape, connectivity, porosity types, and differences in rock fabric and texture. They did so through the use of a parameter called the flowing fraction, which represents the fraction of pore structure contributing to fluid flow. These flowing fractions were obtained from tracer

concentration profiles generated for six different carbonate rock types. In addition, acidization experiments were performed and a master curve (at 150 °F using 15 wt% HCl), **Fig. 1.8**, was then created to show how the optimal pore volumes to breakthrough values are correlated to the flowing fraction. Further experiments were conducted to confirm that this master curve exists under different injection temperatures as well. Each of these master curves exhibits an optimal Damköhler number when the pore volumes to breakthrough value is minimal.

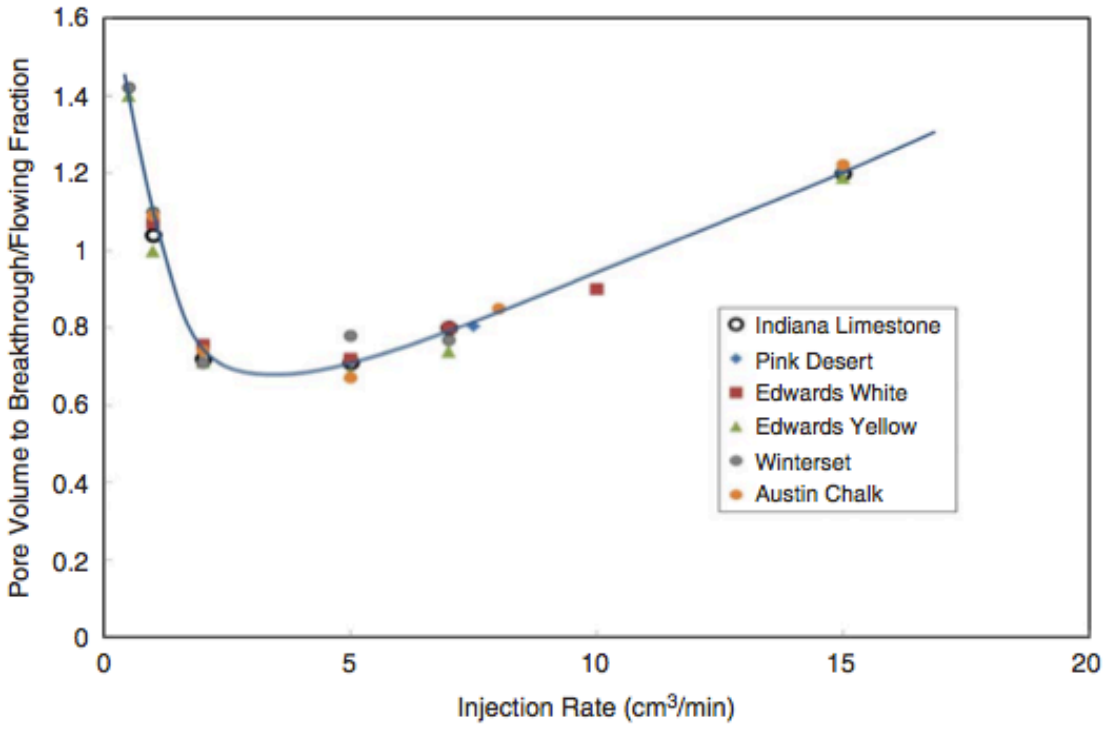

Figure 1.8- Master wormhole efficiency curve for different carbonate rock types based on their flowing fraction (Zakaria et al., 2015).

While studies regarding the effect of permeability on wormhole efficiency have been completed, the range of permeabilities tested has been limited. Furthermore, the combined effect of permeability and pore structure has not been discussed.

1.4 Research Objectives

In this work, core samples with a wide range of permeability will be used to investigate wormhole behavior as permeability and pore structure changes. The objectives of this research include the following:

1. Observe how permeability affects the optimum interstitial velocity
    - Run linear coreflood experiments on limestones with average permeabilities of approximately 6, 11, 33 and 239 millidarcy.
2. Isolate the effects of permeability and porosity using thin section analysis
    - Observe and compare the pore structure and connectivity of the four different limestones.

2. EXPERIMENTAL APPARATUS

This chapter provides an overview of the coreflooding equipment setup (Section 2.1) followed by detailed explanations of specific equipment (Sections 2.2 – 2.7).

2.1 Experimental Apparatus Overview

Grabski (2012) initially designed the setup for these experiments, **Fig. 2.1**. The apparatus consists of syringe injection pump, accumulation system, core holder, hydraulic pump, backpressure regulator, and data acquisition system.

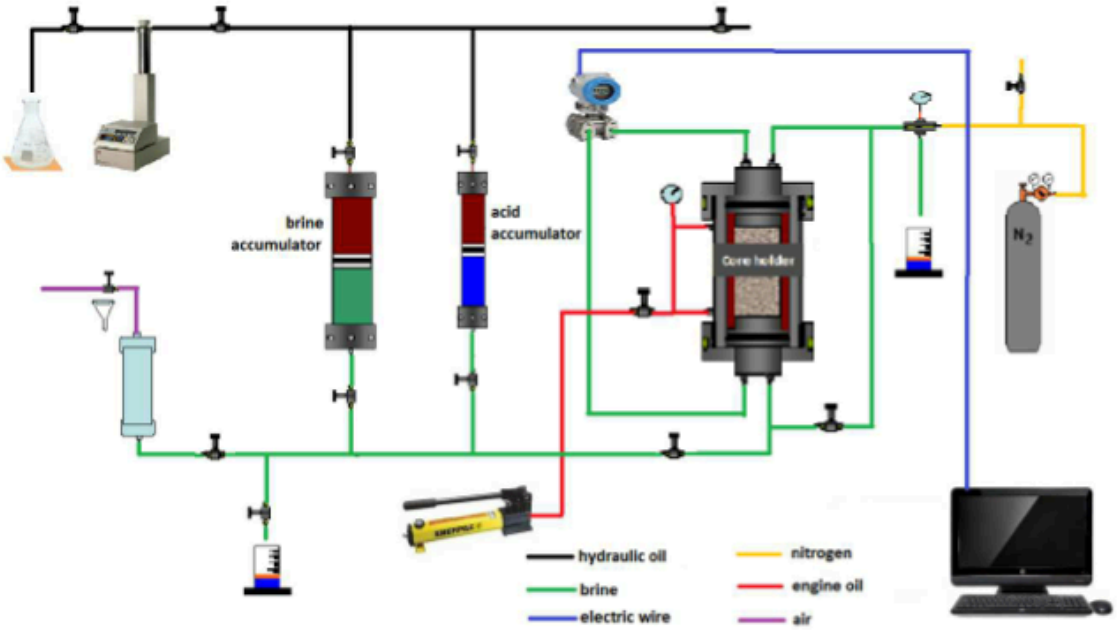

Figure 2.1 – Coreflood system schematic (Dong, 2012).

2.2 Syringe Pump

The Teledyne ISCO syringe pump, shown in **Fig. 2.2**, is used to pump the displacement fluid, hydraulic mineral oil, during the experiment at a controlled flow rate. The pump is capable of injecting flow rates between 0.0001 mL/min to 107 mL/min with a maximum operating pressure of 7,500 psi. However, to achieve a continuous flow rate during experiments, a maximum injection rate of 50 mL/min must be used as the refill rate, 100 mL/min, must be twice as fast as the injection rate.

Mineral oil is pumped to one of the two 260 mL accumulators. This dual pump system allows for continuous fluid flow during experiments, as there is no need to stop and refill the pump. The digital control panel on the pump allows for selection between pumping at a constant pressure or in the case of the designed experiments, constant flow rate. In addition, it displays the flow rate, injection pressure, time, and fluid volume present in the accumulators.

Hydraulic oil or water can be used as the displacement fluid with this syringe pump. Hydraulic oil is used in these experiments.

Figure 2.2- Teledyne ISCO syringe pump (Grabski, 2012).

2.3 Accumulation System

Two accumulators, as shown in **Fig. 2.3,** are used to store brine and acid during experiments. Accumulators are used to prevent pressure surges and protect the pump from corrosive fluids and the possibility of flowback. The accumulators used are manufactured by Phoenix Instruments. They have a maximum pressure rating of 5,000 psi and volume capacity of one liter each. The acid accumulator is composed of Hastelloy C-276, an alloy that is corrosion resistant to oxidizing agents such as hydrochloric acid. The brine accumulator is composed of stainless steel 316.

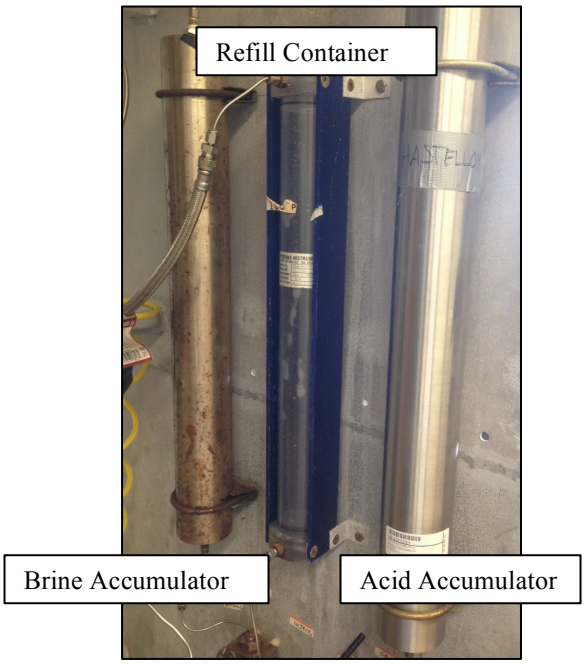

Figure 2.3- Accumulation system.

The accumulators contain a piston that separates displacement fluid from the desired injection fluid (either acid or brine). When the syringe pump is running, displacement fluid is injected into the top of the accumulator which pushes down on the piston and therefore forces the injection fluid out into the flow lines. The accumulators are controlled by two-way values on both the inlet and outlet to prevent the mixing of brine and acid.

In between the two accumulators is a PVC refill container, which is resistant to most acid corrosion. It operates with a pressure limit of 100 psi and has a volume capacity of one liter. This refill container is filled with fluid prior to filling the accumulators. A laboratory air source is connected to the top of the container. This air

source is used to increase the displacement rate of fluid from the refill container. On the bottom of the refill container, three values are present- one for each accumulator and a release value to a waste container for air and excess fluids.

2.4 Core Holder

The core holder, shown in **Fig. 2.4** is a metallic cylinder manufactured by Phoenix Instruments. The core is placed inside and confining pressure is applied to the Viton rubber sleeve within the holder. The holder is composed of Hastelloy C276, a nickel- molybdenum-chromium alloy that is corrosion resistant. It has a maximum pressure rating of 3,000 psi and a maximum temperature rating of 300 °F. For these sets of experiments, a 1.5 inch diameter by 20 inch length core holder is used.

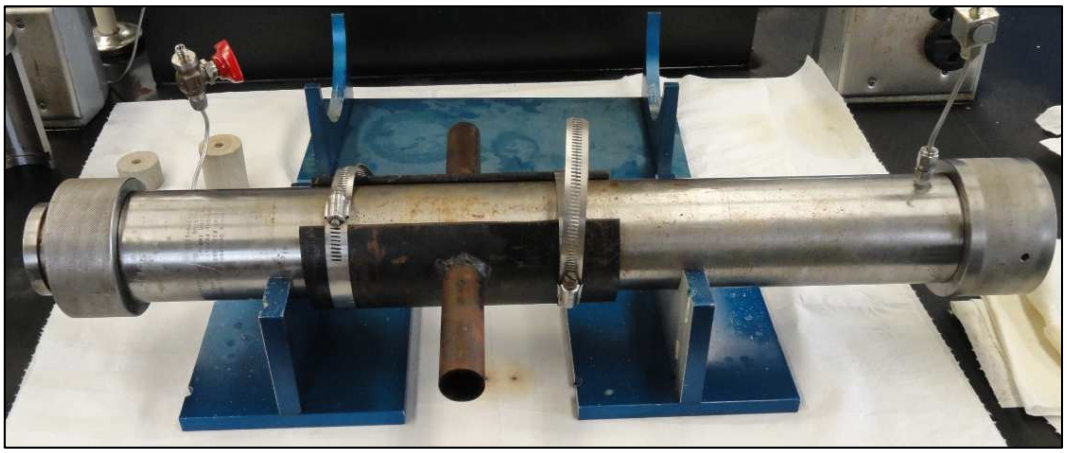

Figure 2.4- Core holder (Dong, 2012).

The core holder consists of three components: the main body, the inlet cap and the outlet cap. The main body contains an inlet connection for confining pressure as well as a release valve for reducing the internal pressure of the core holder. The inlet cap, shown in **Fig. 2.5a**, is placed on the bottom of the core holder and contains a fluid inlet line from the accumulators and a pressure transducer line. The outlet cap, shown in **Fig. 2.5b**, is placed on the top of the core holder and contains a fluid outlet line to a waste container and a pressure transducer line. Metal spacers are connected to the outlet cap to allow for the use of 12 inch cores as in these experiments. A metal screw on sealing cap, shown in **Fig. 2.5c**, is placed over the outlet cap. This creates a tight seal and prevents the outlet cap and injection fluid from being ejected from the core holder when confining pressure is applied.

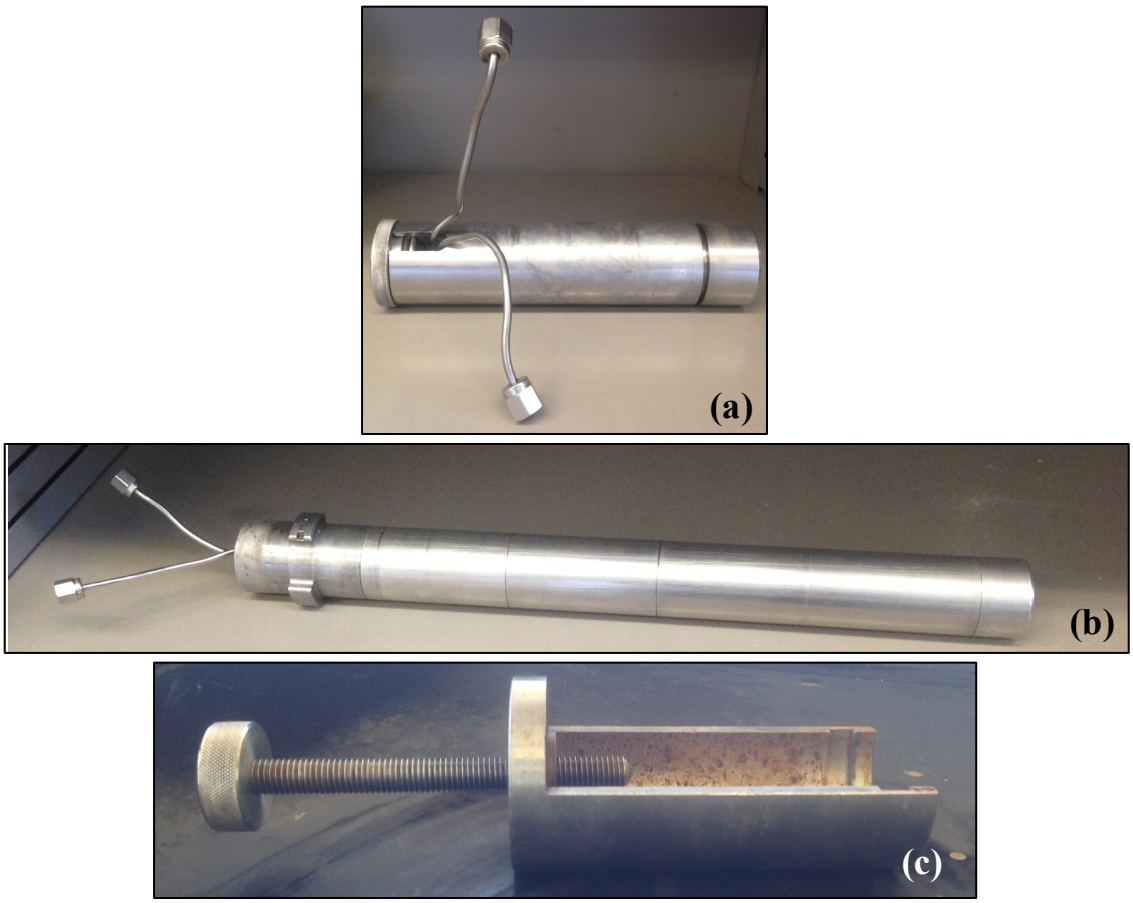

Figure 2.5- Core holder caps.

2.5 Hydraulic Hand Pump

The Enerpac model 392 hydraulic pump in **Fig. 2.6**, is used to apply confining pressure. It has a maximum pressure rating of 10,000 psi and can store 901 mL of fluid. AW32 hydraulic oil is used for the pump. When needed, this oil is hand pumped between the core holder and the Viton rubber sleeved to provide confining pressure to the core. A pressure gauge connected to the core holder is used to monitor confining pressure throughout experiments.

Figure 2.6 - Hydraulic hand pump (Enerpac, 2015).

2.6 Backpressure Regulation

An Equilibar EB1HP1-SS316 backpressure regulator, **Fig. 2.7**, is used to control the pressure at the core outlet and maintain a desired pore pressure. The backpressure regulator is composed of stainless steel and has a pressure rating of 3,000 psi. A stainless steel diaphragm with an additional 50 psi operating pressure is used.

Figure 2.7- Equilibar backpressure regulator (Equilibar, 2015).

To keep the carbon dioxide reaction product in solution and prevent gaseous formation, the backpressure is maintained at 1,500 psi in these experiments. Downhole reservoir conditions reflect pressure values much higher than this, which cannot be achieved under lab conditions due to equipment constraints.

The internal structure of the backpressure regulator is shown in **Fig. 2.8**. A manual pressure regulator (nitrogen tank) is used for these experiments. The regulator is divided into a section on top called the dome and a separate compartment below. The dome connects to a pressure gauge and a nitrogen supply line. A compressed nitrogen gas tank provides the desired pressure to the dome. The compartment below the dome contains an inlet and outlet for the injection fluid. The backpressure regulator works through a balance of pressures on the diaphragm located between the dome and bottom compartment. When the fluid inlet pressure exceeds the dome pressure, which is set by the nitrogen tank, the diaphragm is pushed upwards, breaking the seal between the diaphragm and orifices. As a result, fluid flows through the backpressure regulator to maintain the desired pressure throughout the system.

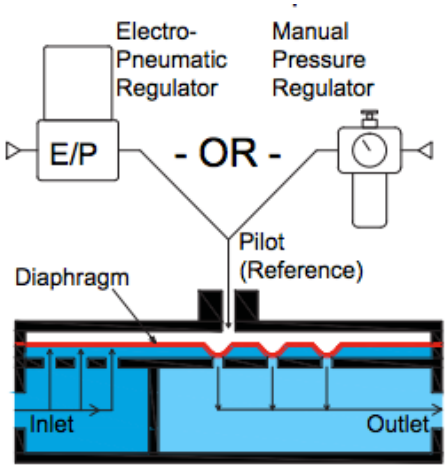

Figure 2.8 - Internal structure of a backpressure regulator (Equilibar, 2015).

2.7 Data Acquisition System

The data acquisition system consists of three components- pressure transducers, a NI signal processing board and a computer with LabVIEW installed. One of two Foxboro pressure transducers, shown in **Fig. 2.9**, is used depending on the pressure differential across the core. One transducer has a pressure range of 0-200 psi while the other has a range of 0-2000 psi. The transducer contains a connection labeled "H" for high pressure (represented by the core inlet/injection pressure) and another connection labeled "L" for the lower pressure (represented by the core outlet). A diaphragm inside the transducers is deflected based on the pressure differential. Based on this deflection, the transducer converts pressure into an electronic signal that is sent to a National Instruments signal processing board. A virtual instrument file, VI file, is generated and is opened using National Instruments' LabVIEW software. As a result, LabVIEW allows

pressure changes to be monitored during experimental runs. LabVIEW generates a text file of data recorded by the second.

Figure 2.9- Foxboro pressure transducer.

3. EXPERIMENTAL PROCEDURE

This chapter provides the details regarding the procedure for core preparation, matrix acidizing itself and post acidization. Section 3.1 provides a summary for the entire core flooding experiment. The following sections provide more details on the major experimental steps. All experiments in this research were run at ambient temperature, approximately 70 °F.

Section 3.13 provides an overview for the thin section experimental procedure.

3.1 Experimental Summary

The general procedure for running experiments is as followed.

1. Dry, weigh and record dry weight of core
2. Saturate the core with clean water in a vacuum pump overnight
3. Weigh and record wet weight of core
4. Calculate core porosity
5. Prepare diluted 15 wt% HCl
6. Fill the acid accumulator with acid and the brine accumulator with water
7. Set up core in core holder and make necessary flow line connections
8. Pump excess air out of the system
9. Set syringe pump to desired flow rate and begin pumping brine through the system
10. Apply 1,500 psi of backpressure using the nitrogen tank

11. Ensure that the confining pressure is always 500 psi greater than the pump injection pressure
12. Wait until the system is pressurized then begin injecting core with brine by turning the bypass valve
13. Use LabVIEW to determine when the pressure across the core has stabilized
14. Calculate permeability using Darcy's Law
15. Begin acid injection while starting a timer at the same time
16. Record the time it takes for wormhole breakthrough, which is determined by monitoring the pressure differential in LabVIEW
17. Close the acid accumulator valve and open the brine valve to flush the system
18. Once the outlet fluid is no longer acidic, stop the injection pump and release the backpressure
19. Remove the core holder and clean the system

3.2 Cores

The cores used for these experiments were purchased from Kocurek Industry Co. They were all cut to the core holder dimensions of 1.5" diameter by 8" length. **Table 3.1** provides an overview of the four different core samples used, including the number of samples. The numbers of samples were limited to the availability of rocks and also the minimum number of experiments necessary to identify the optimal conditions. In this study, four different groups of cores were tested. The main difference between them is

permeability. Also, one set of cores is Desert Pink limestone while the other three groups are Indiana limestones.

Table 3.1 - Summary of core properties.

			
Name: Indiana Limestone **Formation:** Bedford **Total Cores:** 11	**Name:** Indiana Limestone **Formation:** Bedford **Total Cores:** 6	**Name:** Desert Pink Limestone **Formation:** Edwards Plateau **Total Cores:** 9	**Name:** Indiana Limestone **Formation:** Bedford **Total Cores:** 6

Table 3.2 summarizes the average permeability and porosity of each group with the standard deviations of each parameter. The average permeability and porosity values listed are calculated over all the cores in each set. Detailed permeability and porosity information of the samples of each permeability group can be found in Appendix A.

Table 3.2- Average pore properties of each set of experiments.

Set	Rock Type	ϕ_{ave} (%)	σ (%)	k_{ave} (mD)	σ (mD)
1	Indiana Limestone	15	0.5	5.9	0.8
2	Indiana Limestone	11	0.8	10.7	2.0
3	Desert Pink Limestone	25	1.2	33.2	5.0
4	Indiana Limestone	16	0.6	239.3	132.2

3.3 Data Recording

A sample data recording worksheet used for data recording for all matrix acidizing experiments is shown in **Table 3.3**. In Table 3.3, information regarding core geometry, porosity, permeability, and acid fluid properties is listed. This data sheet is available for each experiment.

Table 3.3- Sample matrix acidizing data worksheet.

Coreflooding Data Sheet

Core#	Core 5	Date	September 3, 2014
Core diameter	1.5 inch		
Core length	8 inch	Acid Coreflooding	
		Temperature	70 °F
Porosity Measurement			
Weight (Dry)	436.44 g		
Weight (Satuated)	496.63 g		
Porosity	25.98%		
Pore Volume	60.19 cm^3	Acid Injection Rate	3.55 cc/min
		Interstitial Velocity	1.20 cm/min
		Volume of Pipe between Core and Acid tank	2.30 cm^3
Permeability Measurement			
Injection Rate	3.55 cc/min		
Pressure Differential	53 psi		
Permeability	29.24 md	Time for Acid to Get the Core	38.8 seconds
Acid Formulation	15 wt% HCl	Time for Acid Injection	2293 seconds
Water	465 cm^3		
HCl (37 wt%)	285 cm^3	Pore Volumes to Breakthrough	2.22 Pore volume

3.4 Core Preparation

Cores are first numbered with a permanent marker to ensure they can be identified throughout the duration of the experiment. Cores are then placed in a lab oven for two hours to remove any moisture present in the pore spaces. Afterwards, the dry weights of the cores are measured using a lab scale and recorded for use in calculating porosity.

Core saturation begins by submerging the cores in brine (water for these experiments) within a glass bell container, **Fig. 3.1a**, or PVC container, **Fig. 3.1b**. The glass bell container is preferred as a tighter seal can be created. However, due to it's smaller volume, if multiple cores are to be saturated at the same time, the PVC container is used. The core must be fully submersed in the brine with an excess of a couple inches of water since the fluid level will decrease as pore space is filled. It is important that the brine is cleaned and free of impurities. Both containers are covered with a lid that attaches to a vacuum pump by a rubber hose, **Fig. 3.1c**.

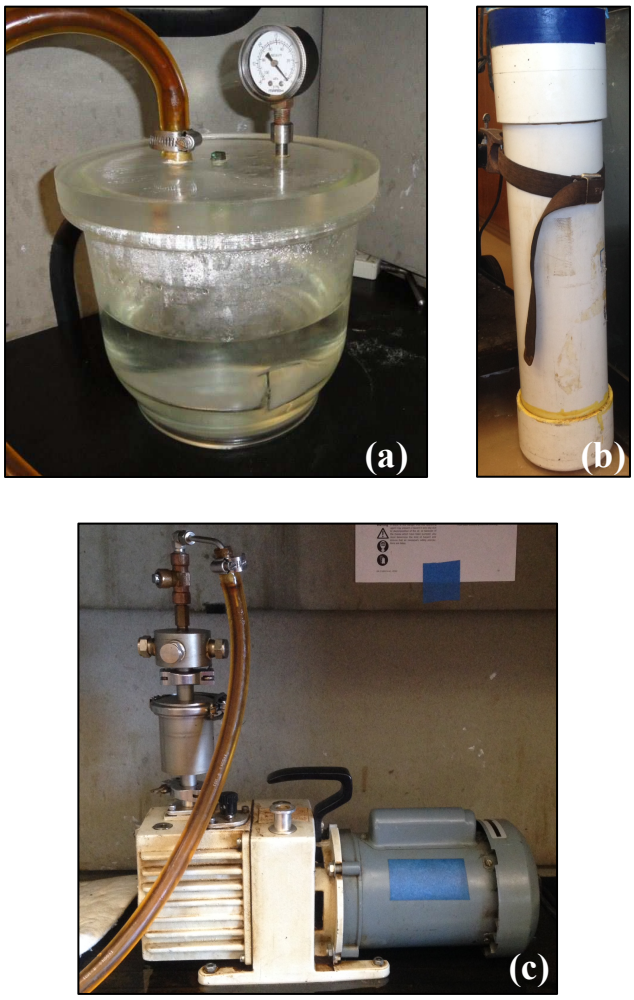

Figure 3.1- Core saturation equipment: (a) glass bell container, (b) PVC container, (c) vacuum pump.

To ensure the creation of a tight seal of the saturation container, an adequate amount of vacuum grease needs to be applied to the container lid. The vacuum pump must be run for at least 10 hours to fully saturate the cores. After saturation, the wet weights of the cores are measured and recorded for use in calculating porosity. The cores should be submerged in the same type of brine in another container until placed in the core holder to prevent changes in core properties.

3.5 Porosity Measurement

Using the recorded dry and wet weights, Eqs. 3.1 – 3.3 calculate the porosity. Porosity needs to be calculated prior to acidizing to determine what acid injection rate should be used.

$$\emptyset = \frac{V_{pore}}{V_{bulk}} \text{ x } 100\% \quad \text{.....(3.1)}$$

$$V_{pore} = \frac{M_{saturated} - M_{dry}}{\rho_{brine}} \quad \text{.....(3.2)}$$

$$V_{bulk} = A \cdot L = \frac{1}{4}\pi d^2 \cdot L \quad \text{..... (3.3)}$$

3.6 Acid Preparation

The lab purchases hydrochloric acid, HCl, manufactured by Macron Fine Chemicals with a concentration of 36.46% by weight. However, an HCl concentration of 15% by weight is desired for these experiments as it is most commonly used in industry practices. Therefore, the stock acid must be diluted. **Table 3.4** provides the acid information necessary for calculating dilution volumes. A total volume of 750 mL experimental HCl acid is created prior to running each set of experiments. This volume ensures there's enough acid for at least three experiments but also prevents wasting excess acid.

Table 3.4- HCl acid volumes for dilution.

Fluid Type	Concentration, weight % (c)	Density, g/cm^3 (ρ)	Volume, mL (V)
Stock HCl acid	36.46	1.18	285
Water	0.00	1.00	465
Experimental HCl acid	15.00	1.07	750

The following calculations are used to calculate the stock HCl acid and water volumes needed to obtain a concentration of 15% by weight HCl.

$$V_{stock} = \frac{V_{experimental} c_{experimental} \rho_{experimental}}{c_{stock} \rho_{stock}} \quad \text{.....(3.4)}$$

$$V_{water} = V_{experimental} - V_{stock} \quad \text{.....(3.5)}$$

3.7 Accumulation System Setup

To prepare the accumulation system for the experiment, several steps must be taken: all excess fluid must be removed from the accumulators, both accumulators must be refilled with fresh injection fluids and any excess air must be pumped out of the system. This is accomplished through the use of the syringe pump, two accumulators, a refill container and a laboratory air source. A schematic of the accumulation system with labeled valves is shown in **Fig. 3.2**. An important thing to remember throughout the experiment that the volume of fluid is added to the system will be displaced in the same volume from the system.

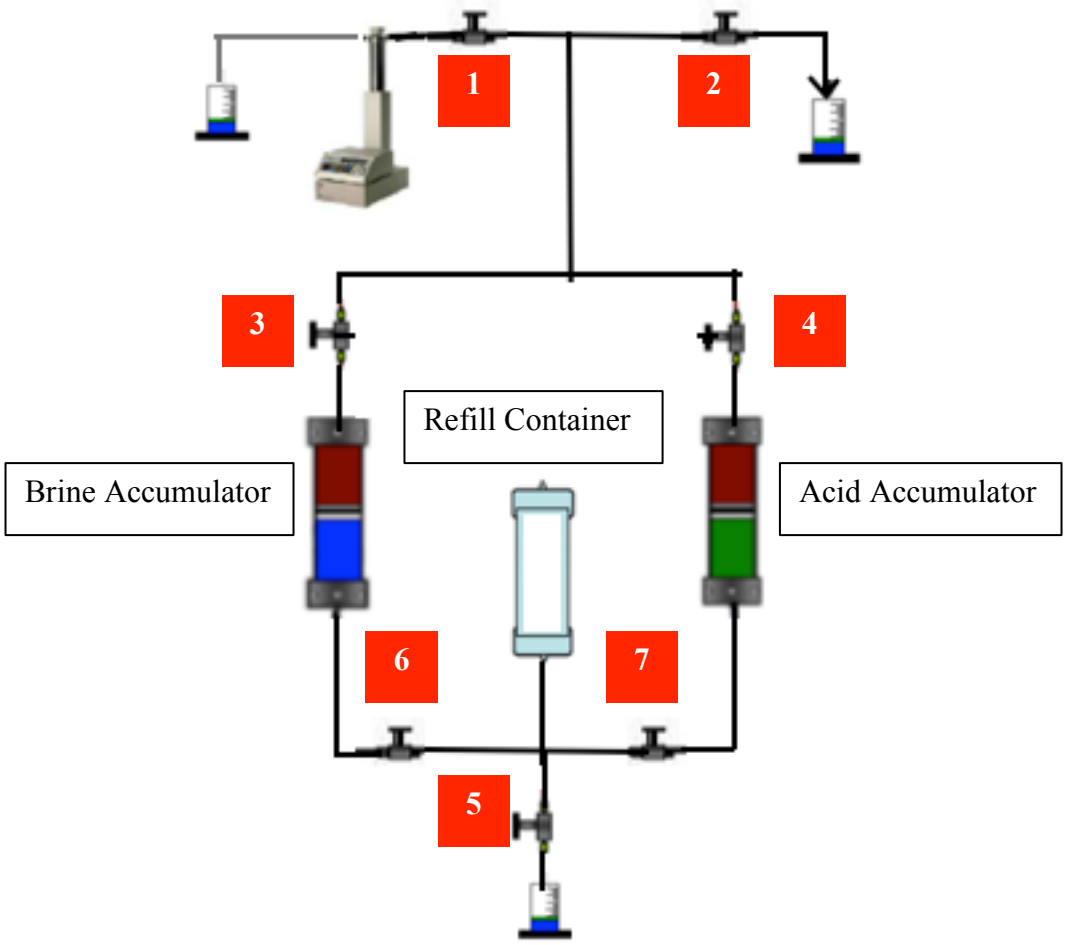

Figure 3.2- Schematic of accumulation system.

Throughout the experiment, valves 1, 3, and 4 are to remain open at all times. All other valves should be closed initially. The following steps are taken to ensure that all excess brine and acid has been removed from the accumulators.

1. Check to make sure all air has been removed from the system by ensuring valve 2, the oil vent valve, is open. Set the syringe pump to a flow rate of 10 mL and

wait for a steady outlet flow. This steady flow indicates that the syringe pump is free of air.

2. To remove all excess acid from the acid accumulator, close valve 2 and open valves 5 and 7. Using the syringe pump, inject at a flow rate between 10-40 mL to pump the excess acid out of valve 5 and into the waste container. When the syringe pump pressure starts to quickly increase and fluid is no longer being expelled, stop the pump immediately. This indicates that the accumulator piston has been pushed to the bottom of the container and the accumulator is now completely filled with displacement fluid from the syringe pump.
3. To remove all excess brine from the brine accumulator, close valve 7 and open valve 6. Use the syringe pump in the same way as in step 2 to empty the brine accumulator. Removing brine after acid is important as it cleans out the system tubing of acidic fluid.

Next, the brine accumulator needs to be refilled by completing the following steps. Distilled water is used as brine in these experiments.

4. Close valve 5 and fill the refill container with 1 L of brine using a funnel. Secure the top with nut.
5. Once the refill container is completely filled, switch value 6 to the refill position (towards the left) and open valve 2. This will allow fluid from the refill container to flow into the brine accumulator through valve 6 while displacement fluid is removed through valve 2.

6. Slowly open the air supply valve slightly. This will provide air pressure to decrease the displacement time of the brine out of the refill container. Be sure to turn off the air supply and then close valve 6 before all the brine has been removed from the refill container to prevent the introduction of air into the system.
7. Open valve 5 to remove excess brine and built up air pressure from the refill container into the waste container.

Now that the refill container is empty once again, the acid accumulator can be filled using the following steps.

8. Close valve 5 and carefully fill the refill container with the previously prepared 15 weight % HCl.
9. Once the refill container is completely filled, open the refill connection of value 7 (on the top) and open valve 2. This will allow fluid from the refill container to flow into the acid accumulator through valve 7 while displacement fluid is removed through valve 2.
10. Slowly open the air supply valve. Once again, be sure to turn off the air supply and then close valve 7 before all the acid has been removed from the refill container.
11. Open valve 5 to empty the refill container into the waste container.

The refill container needs to be cleaned via the following steps prior to proceeding with the rest of the experiment.

12. Close valve 5 and fill the entire refill container with water.

13. Open valve 5 and apply the air source to force water into the waste container.
14. Repeat steps 12-13 (usually two to three times) until pH strips identify a waste fluid stream of a neutral pH.

Finally, ensure there is no air in the system and flush the tubing of acid using the following steps.

15. Close valves 2, and 6. Open valve 5 and turn valve 7 to the inject position (on the bottom). Set the syringe pump to an injection rate of 10 mL/min and watch for a steady flow of acid through valve 5 into the waste container.
16. Once a steady flow is observed, stop the pump. Close valve 7 and turn valve 6 to the inject position (towards the right). Set the syringe pump to an injection rate of 10 mL/min and watch for a steady flow of water through valve 5 into the waste container. Run the pump until pH strips indicate a neutral pH to ensure the tubing is flushed of acid. This concludes the accumulation system set up procedure.

3.8 Core Holder Setup

After cleaning the interior of the core holder with paper towels, insert the core in the core holder. If necessary, add spacers to the outlet cap. Spacers are important as they prevent the rubber sleeve within the core holder from breaking under the applied confining pressure. Once the inlet cap, outlet cap and outlet sealing cap are attached, mount the core holder vertically on the experimental shelf with the outlet on top. To remove fluid flow path inconsistency amongst experiments, tie a strap around the top of the outlet sealing cap to prevent the core holder from leaning forward. A schematic of

the core holder connections is provided in **Fig 3.3**. When making connections, it is important to use thread seal tape to reduce undesired pressure loses within the system. Be sure to not block any of the flow path with the tape.

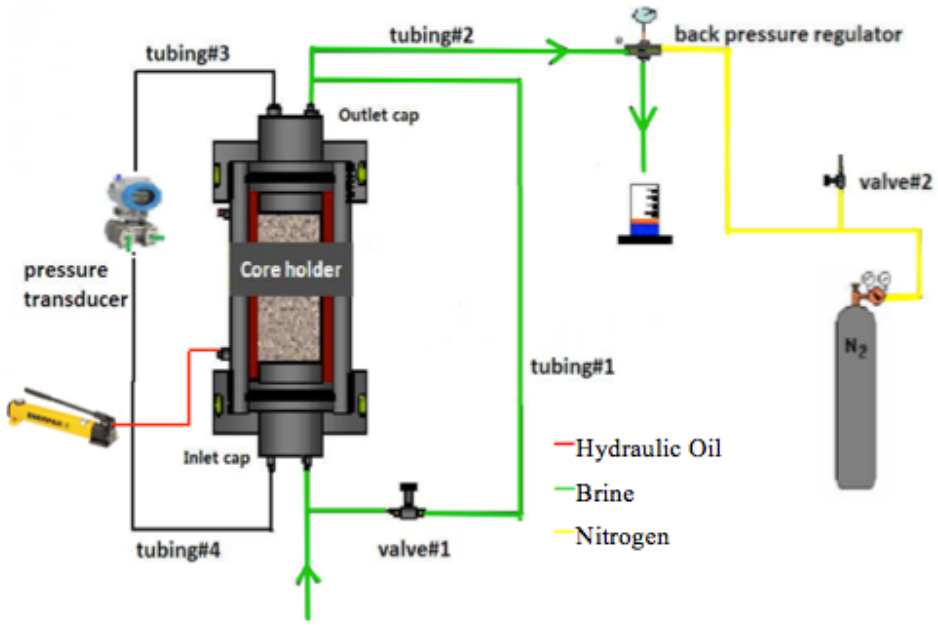

Figure 3.3- Core holder connections schematic.

The core holder inlet is connected to the high-pressure port of the pressure transducer and the inflow fluid line. The core holder outlet is connected to the low-pressure port of the pressure transducer and the backpressure regulator. The confining pressure flow line is connected to the core holder body. Tubing #1 serves as bypass tubing during the experiment once confining pressure has been applied to the core holder. When valve #1 is open, tubing #1 allows fluid to fill and pressurize the entire system before injecting into the core.

3.9 Pressure Build Up and Permeability Test

Once all the tubing is connected, the system needs to be pressurized. A permeability test is then performed on the core through the following steps. The valves and tubing discussed in this section correspond to the labeling in Fig. 3.3 unless otherwise specified.

1. Apply confining pressure to the core holder using the hydraulic hand pump. To do this, make sure the release valve on the core holder body is open and the release valve (valve A) on the hydraulic hand pump in closed (**Fig. 3.4**). Pump until oil comes out of the core holder release valve at a steady rate. This ensures that all air trapped between the core holder body and the rubber sleeve is removed. Close the release valve on the core holder body to allow the confining pressure to build up. Pump hydraulic oil to the core holder until a confining pressure of 400- 500 psi is obtained. Confining pressure prevents injected fluid from bypassing the core.

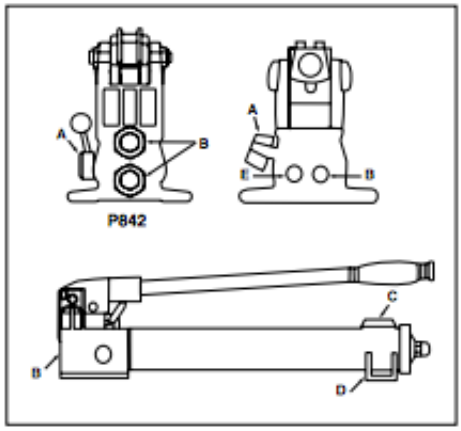

Figure 3.4- Hydraulic hand pump valves (Enerpac, 2015).

2. Open valve #1 so the brine will flow through tubing #1 rather than through the core. Set the syringe pump to an injection rate of 10 mL/min. This flow rate is used because it allows the system to be pressurized in a reasonable amount of time while not putting too much stress on the backpressure regulator. Set the brine accumulator valve to inject and run the pump until a steady flow of fluid emerges from the backpressure regulator. This ensures all air is out of the system and provides time for all tubing to be filled with brine at atmospheric pressure.
3. Next, backpressure is applied using the nitrogen tank. Backpressure keeps the carbon dioxide reaction product in solution and simulates pressure closer to reservoir conditions. Open the valve to the nitrogen tank to apply 1,500 psi of pressure. Brine will stop flowing out of the backpressure regulator since the backpressure (dome pressure) is greater than the inlet pressure. This results in the diaphragm sealing off the orifices that allow fluid to flow through the regulator. Continue to run the syringe pump until the injection pressure is greater than the backpressure and fluid flows out of the backpressure regulator. It will take some time for the syringe pump to build up enough pressure to exceed the backpressure. If fluid emerges from the backpressure regulator before the syringe pump pressure is higher than the backpressure, the backpressure regulator is not working properly. If this is the case, stop the syringe pump immediately. Usually the diaphragm will need to be replaced. While waiting for the syringe pump to build up pressure, the following steps should be taken to ensure the experiment is running correctly.

a. Check all connections for any leaks using a paper towel. Some leaks cannot be detected until the system is highly pressurized. If leaks are present, stop the syringe pump, depressurized the system (which is explained in detail in Section 3.11), and make the necessary repair. If tightening the connections does not stop the leak, the nut and ferrule of the faulty connection needs to be replaced.
b. Keep the confining pressure 400-500 psi greater than the syringe pump pressure at all times.
c. Especially when running low permeability cores, ensure that the syringe pump pressure does not exceed 2000 psi (due to pressure transducer constraints). If pressure starts to approach this limit, stop the syringe pump immediately.
d. To double check if there is any air in the system, test the flow rate coming out of the backpressure regulator using a graduated cylinder and a stopwatch. The outlet flow rate should equal the syringe pump injection rate. If the flow rates are not equal, the system needs to be checked for leaks and/or flushed out to ensure no air is present.

4. Once the system is fully pressurized the permeability test can be performed. Set the syringe pump to the desired injection flow rate. Wait until there is steady fluid outflow at the backpressure regulator.

5. Open and start running Labview to view the pressure differential across the core. Close valve #1 to allow brine to be injected through the core. A typical pressure buildup curve is provided in **Fig. 3.5**. The pressure differential will increase quickly until the flow reaches steady state. Steady state is identified when the pressure differential remains relatively constant. Record the pressure differential at steady state flow.

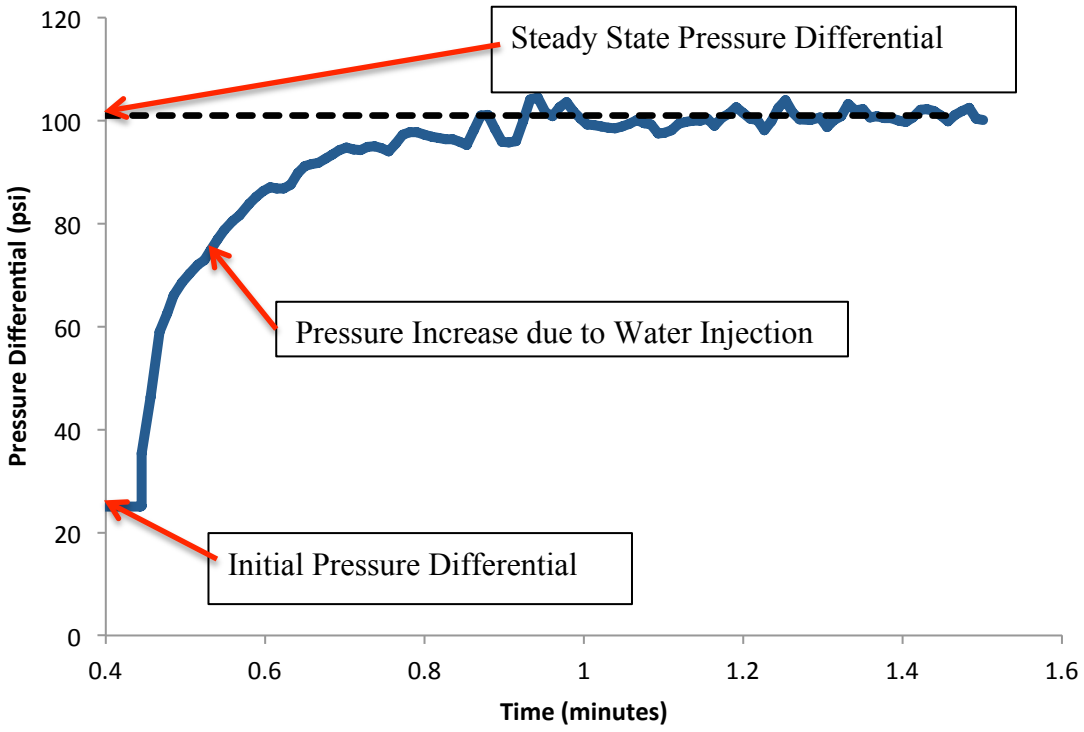

Figure 3.5- Typical pressure buildup curve due to water injection.

Permeability is calculated using Darcy's Law (Eqs. 3.6 and 3.7). To calculate the change in pressure, Δp, used in Darcy's Law, subtract the initial pressure differential from the pressure differential at steady state.

In standard oil field units: $k = \frac{q*L*\mu}{\Delta p*A}$ ……(3.6)

Using experimental units: $k = \frac{122.63*q*L*\mu}{\Delta p*d^2}$ ……..…….(3.7)

Where q is in cm^3/min, L is in inches, μ is in cp (and equal to one centipose for water), p is in psi and d is in inches in Equation 3.7. The conversion factors used to obtain Equation 3.7 are provided in Appendix B.

3.10 Acidizing Procedure

The next major step of the experiment is to acidize the core and determine the time for wormhole breakthrough. **Fig. 3.6** and the following steps provide more details on this procedure.

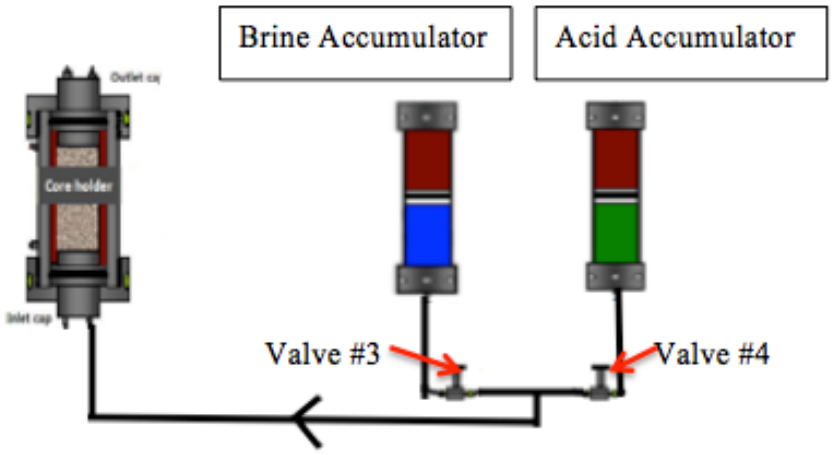

Figure 3.6- Schematic of injection valves.

The following steps must be done as quickly as possible to prevent the mixing of brine and acid. Since the syringe pump remains running during the entire procedure, one of the two accumulator valves must be open at all times.

1. Quickly turn the inject dial (on the bottom) of valve #4 while starting a stopwatch to record time for the wormhole breakthrough.
2. Close valve #3 as quickly as possible.
3. Monitor the change in the pressure differential across the core using LabVIEW. There will be a sharp drop in pressure once the wormhole begins to grow along the core and creates a less restrictive flow path. Record the time it takes for the wormhole to breakthrough. Wormhole breakthrough is indicated by a negligible pressure drop and steady state acid outlet flow. Based on experience, this occurs around 25 psi for the low permeability samples and 6 psi for the 239 mD sample.

4. After wormhole breakthrough is apparent, inject brine again to flush out the system. To do this, first turn valve #3 to the inject position (towards the right) and then close valve #4.

3.11 Depressurizing and Cleaning System

Once acidizing is complete, the system needs to be depressurized and flushed of acid by following these steps.

1. Continue to inject brine through the system until the fluid coming out of the backpressure regulator is not longer acidic. This reduces the chance of pipe corrosion.
2. Depressurizing the system must be done carefully. First, slowly open the nitrogen gas vent valve slightly to release some of the backpressure. Close the nitrogen tank valve partly and then release the confining pressure by turning the release valve on the hydraulic hand pump.
3. Once the confining pressure is released, close the nitrogen gas valve all the way to release all the backpressure. Now the core holder connections can be disconnected and the core removed. Be sure to wash both the core and core holder caps with water. Clean the interior of the core holder body with paper towels.
4. If acid is still present in the acid accumulator, it needs to be removed as described in Section 3.7. Brine must then be run through the system to completely flush out the acid.

5. Be sure to dispose of the contents in any of the experimental waste containers in a labeled acid disposal container.

3.12 Pressure Analysis

Understanding pressure values throughout the system is very important. Not only is it important for data collection, it helps with troubleshooting the system and determining if experiments are valid. The different pressures present in the fully pressurized system are shown in **Fig. 3.7** and explained below.

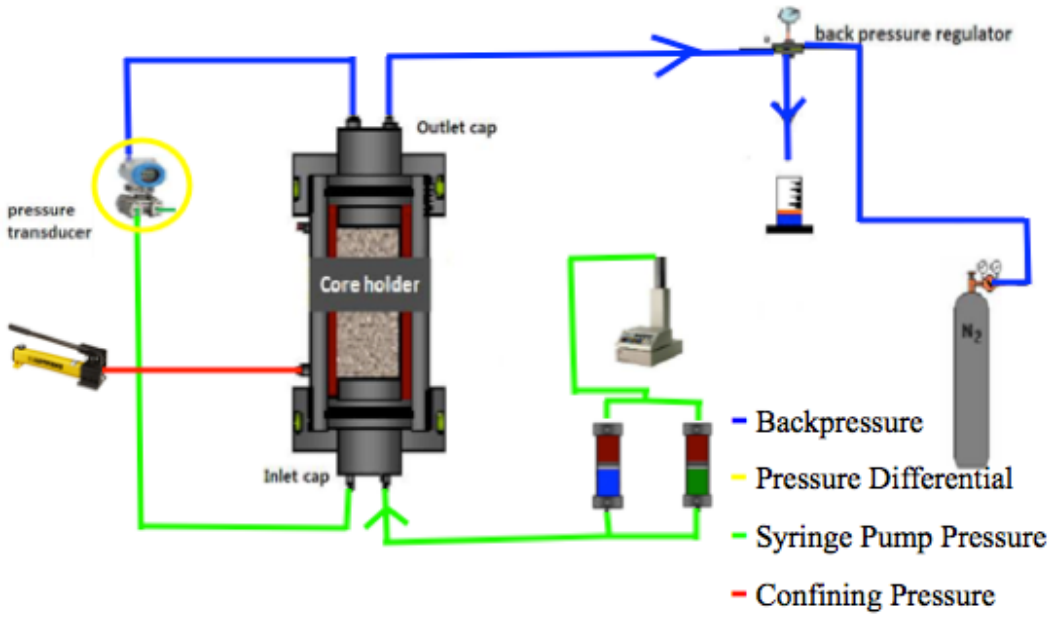

Figure 3.7 - Schematic of pressurized system.

The pressure at the outlet of the core equals the backpressure supplied by the nitrogen tank (indicated by the blue flow line). The backpressure remains at a set constant

pressure of 1,500 psi during the entire experiment. This is also the core pore pressure. The pressure transducer records the pressure differential (indicated by the yellow circle) between the inlet and outlet of the core. The pressure at the core inlet (indicated by the green flow line) equals the syringe pump pressure. This pressure is equivalent to the backpressure plus the pressure differential across the core. Finally, the confining pressure from the hydraulic pump is adjusted to always be 400-500 psi above the syringe pump injection pressure to prevent fluid from bypassing the core.

3.13 Thin Section Analysis

In addition to the coreflood acidization experiments, pore structure and the largest surface pore were studied by thin section analysis. Thin sections were cut from the same limestone samples used for the coreflood experiments. These thin sections were 2 inches wide by 3 inches long and 30 micrometers thick. The pores were colored with blue dye. To study the pore structures, the thin sections were scanned under a regular image scanner.

4. RESULTS AND DISCUSSION

Pore volumes to breakthrough values are calculated with the experimental data for each core. Section 4.1 provides detailed calculations on obtaining this value. To generate enough data to determine the optimum interstitial velocity, injection rates from all three flow regimes must be selected. As described in Section 4.2, once enough data as been generated, the Buijse-Glasbergen model fits the experimental data and ultimately predicts the optimum interstitial velocity. Section 4.3 presents the results obtained regarding the effect of permeability on the optimal wormholing conditions. Section 4.4 provides thin section images and observations regarding the effect of pore structure on the optimal wormholing conditions.

4.1 Determining Pore Volumes to Breakthrough

The goal of this research is to find the optimum interstitial velocity for each of the four sets of permeability-varied limestones. The first step in determining this value involves calculating the pore volumes to breakthrough and interstitial velocity for each experiment.

Interstitial velocity, v_i, is defined as the velocity of the injected fluid through the pore space cross sectional area (Eq. 4.1). Details regarding Equation 4.2 are provided in Appendix B.

$$v_i = \frac{q}{A * \phi} \quad \text{.....(4.1)}$$

$$v_i = \frac{q}{(5.067 * d^2 * \phi)} \quad \text{.....(4.2)}$$

The pore volumes to breakthrough, PV_{bt}, is defined as the amount of acid required to breakthrough the core in terms of pore volumes. It is a dimensionless value, allowing easy for comparison amongst experiments. The following equation calculates the pore volumes to breakthrough.

$$PV_{bt} = \frac{V_{acid}}{V_{pore}} = \frac{q * t}{V_{pore}} \quad \text{.....(4.3)}$$

The following steps and provided acidization pressure curve, **Fig. 4.1**, allow for the calculation of injection time, t.

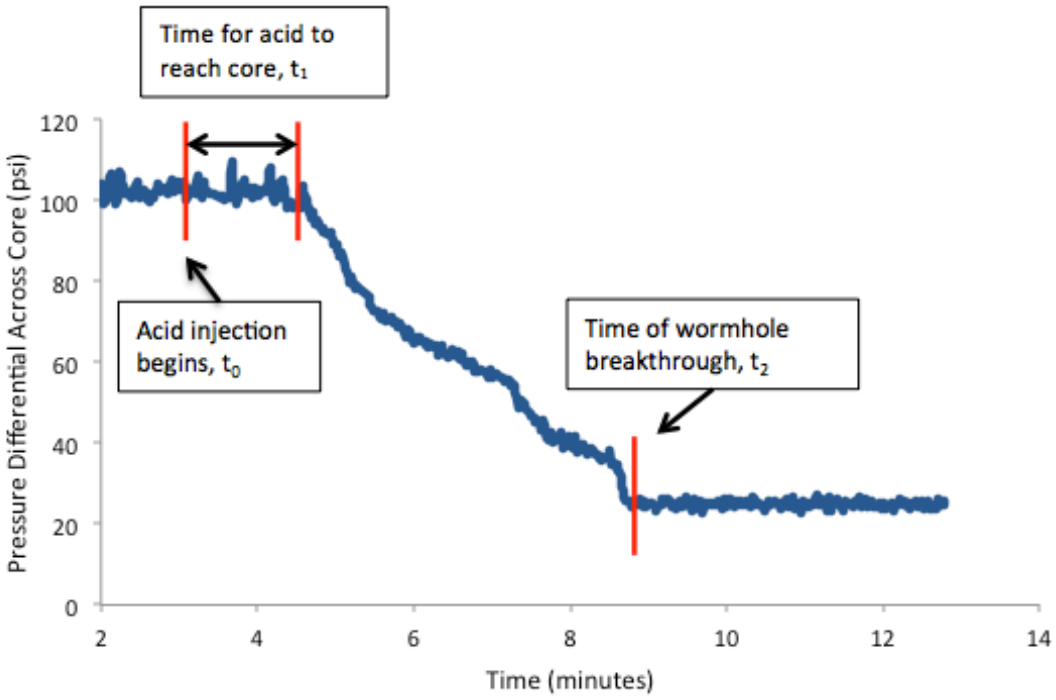

Figure 4.1- Typical acidization pressure curve with critical times.

1. Once the acid accumulator valve is turned to inject and the stopwatch has been started, record the time as t_0.
2. Determine the time it takes for the acid to reach the core based on the acid injection rate and the volume of tubing between the accumulator and core inlet. The following equation calculates the volume of tubing.

$$V_{tubing} = L_{tubing} * 5.067 * ID^2 \quad \text{.....(4.4)}$$

The length of the tubing is measured by a tape measure in centimeters and the inner diameter of the tubing, ID, is provided by the manufacture (in inches). More detail regarding Equation 4.4 is provided in Appendix B.

Next, calculate the time it takes for the acid to reach the core with the following equation.

$$t_1 = \frac{V_{tubing}}{q} \quad \text{.....(4.5)}$$

3. Once the wormhole has broken through the core (indicated by a negligible pressure drop and steady state acid outlet flow), record the time as t_2.
4. Injection time is then calculated using the following equation.

$$t = t_2 - t_1 - t_0 \quad \text{.....(4.6)}$$

5. Use Eq. 4.3 to calculate the pore volumes to breakthrough.

4.2 Determining Optimum Interstitial Velocity

Each experiment generates one data point (pore volumes to breakthrough vs. interstitial velocity). For example, **Table 4.1** provides the experimental data for the Desert Pink limestone set of experiments. There are nine experiments in this data set. The injection rate was the changed parameter for each experiment. Raw experimental

data for the other limestone sets is provided in Appendix A. Careful selection of the acid injection rate must be done to ensure collection of data from all three flow regimes. Injections rates that are low (surface dissolution pattern), medium (optimum condition) and high (uniformed branched pattern) must be selected to generate the wormhole efficiency curve.

Table 4.1- Desert Pink (33 mD) experimental data.

Core#	Permeability (mD)	Porosity	Acid injection rate (ml/min)	Interstitial Velocity(cm/min)	PV_{bt}
1	39.33	25%	10.00	3.46	0.68
2	29.24	26%	3.55	1.20	2.22
3	38.51	26%	9.35	3.20	0.70
4	29.98	23%	16.00	6.01	0.69
5	35.28	23%	8.15	3.06	0.74
6	25.62	24%	3.58	1.32	2.56
7	28.15	24%	4.90	1.80	1.01
8	35.10	25%	19.70	7.03	0.72
9	37.62	26%	6.55	2.22	0.89
Average	*33.20*	*25%*	-	-	-

The experimental data is plotted on a log-log plot to obtain **Fig. 4.2**.

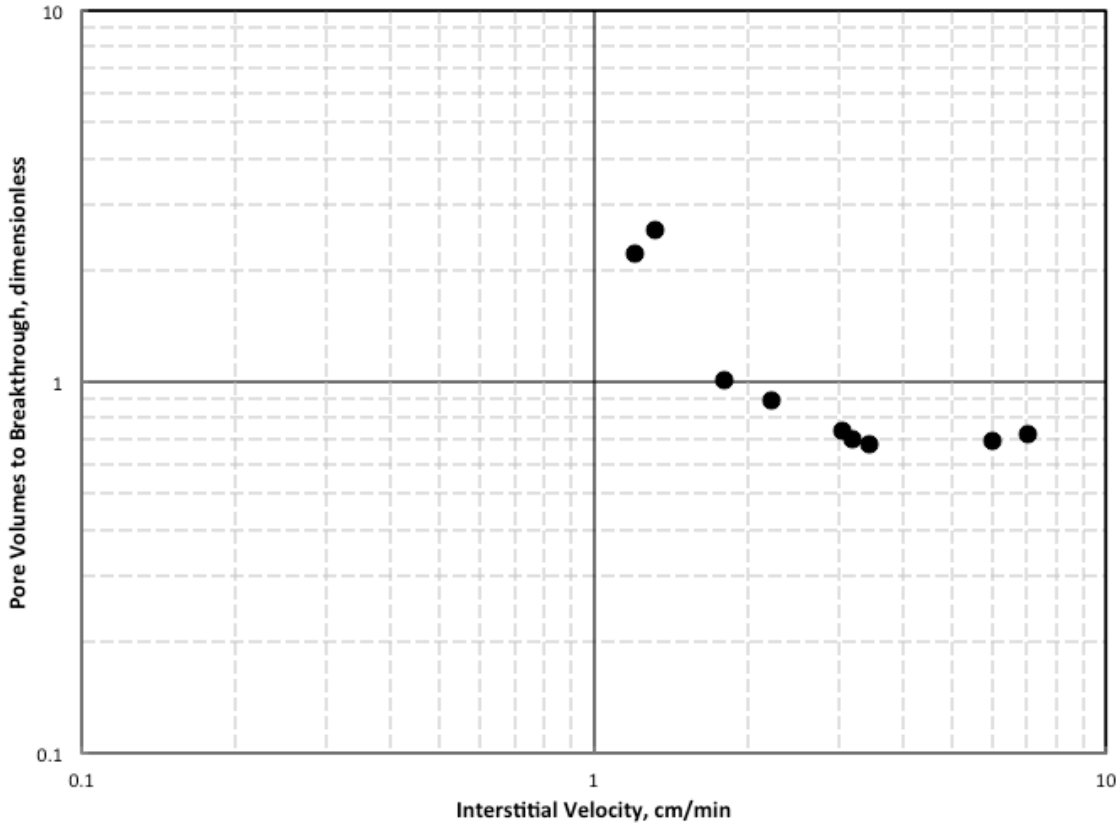

Figure 4.2- Desert Pink experimental data.

Once plotted, the data needs to be curve fitted to determine the optimum interstitial velocity. As discussed in Chapter 1, the Buijse-Glasbergen semi-empirical model successfully curve fits the data. Eqs. 4.7- 4. 10 explain the model.

$$PV_{bt} = \frac{v_i^{1/3}}{W_{eff} * B(v_i)} \quad \text{.....(4.7)}$$

$$W_{eff} = \frac{v_{i-opt}^{1/3}}{PV_{bt-opt}} \quad \text{.....(4.8)}$$

$$B(v_i) = (1 - \exp(-W_B * v_i^2)^2 \quad \text{..... (4.9)}$$

$$W_B = \frac{4}{v_{i-opt}^2} \quad \text{.....(4.10)}$$

The wormhole efficiency factor, W_{eff}, and the wormhole B-factor, W_B, are constants related to the optimal conditions. Eq. 4.9 represents the B-function, which describes the compact dissolution regime that occurs during low acid injection rates. By combining Eqs. 4.7 – 4.10, the following relationship between pore volumes to breakthrough and interstitial velocity is obtained.

$$PV_{bt} = PV_{bt-opt}\left(\frac{v_i}{v_{i-opt}}\right)^{1/3}\left\{1 - \exp\left[-4\left(\frac{v_i}{v_{i-opt}}\right)^2\right]\right\}^{-2} = f(v_i) \quad \text{.....(4.11)}$$

Experimental data provides the PV_{bt} and v_i values in Eq. 4.11**.** The wormhole efficiency factor, W_{eff}, and the wormhole B-factor, W_B, are constants determined experimentally by numerically fitting Equation 4.11 to the results of the coreflood experiments. By using a least square method to minimize error, Eq. 4.12, the experimental data is fitted and the optimal conditions are solved for.

$$J = \sum_i^n \left[PV_{bt}^i - f(v_i^j)\right]^2 \quad \text{.....(4.12)}$$

Where n represents the number of experiments.

Using the Microsoft Excel solver feature, the J function is minimized to determine $PV_{bt\text{-}opt}$ and $v_{i\text{-}opt}$, as shown in **Fig. 4.3**.

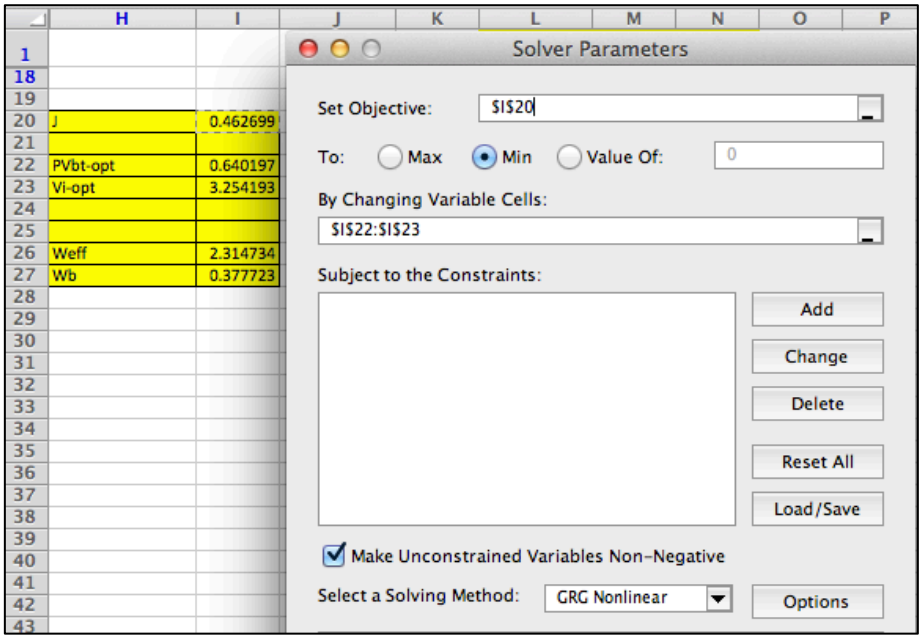

Figure 4.3- Using Excel Solver to solve for optimal conditions.

A simpler method is to directly solve for W_{eff} and W_B using Eq. 4.8 and Eq. 4.10. However, this method is much less accurate than a direct curve fit.

Once the optimum condition is solved for, the data and fitted curve are plotted in Excel. Section 4.3 presents the curve fitted results for each set of experiments.

4.3 Effect of Permeability on Optimal Conditions

Four sets of cores of varied permeabilities were acidized to investigate the effect of permeability on the optimum interstitial velocity and pore volumes to breakthrough.

As stated in Section 4.3, the Buijse-Glasbergen semiempirical model was used to fit the experimental data and to determine the optimal conditions. **Fig 4.4** presents the curve fitted experimental results. Dong (2012) conducted the experiments for the 6 mD Indiana limestone.

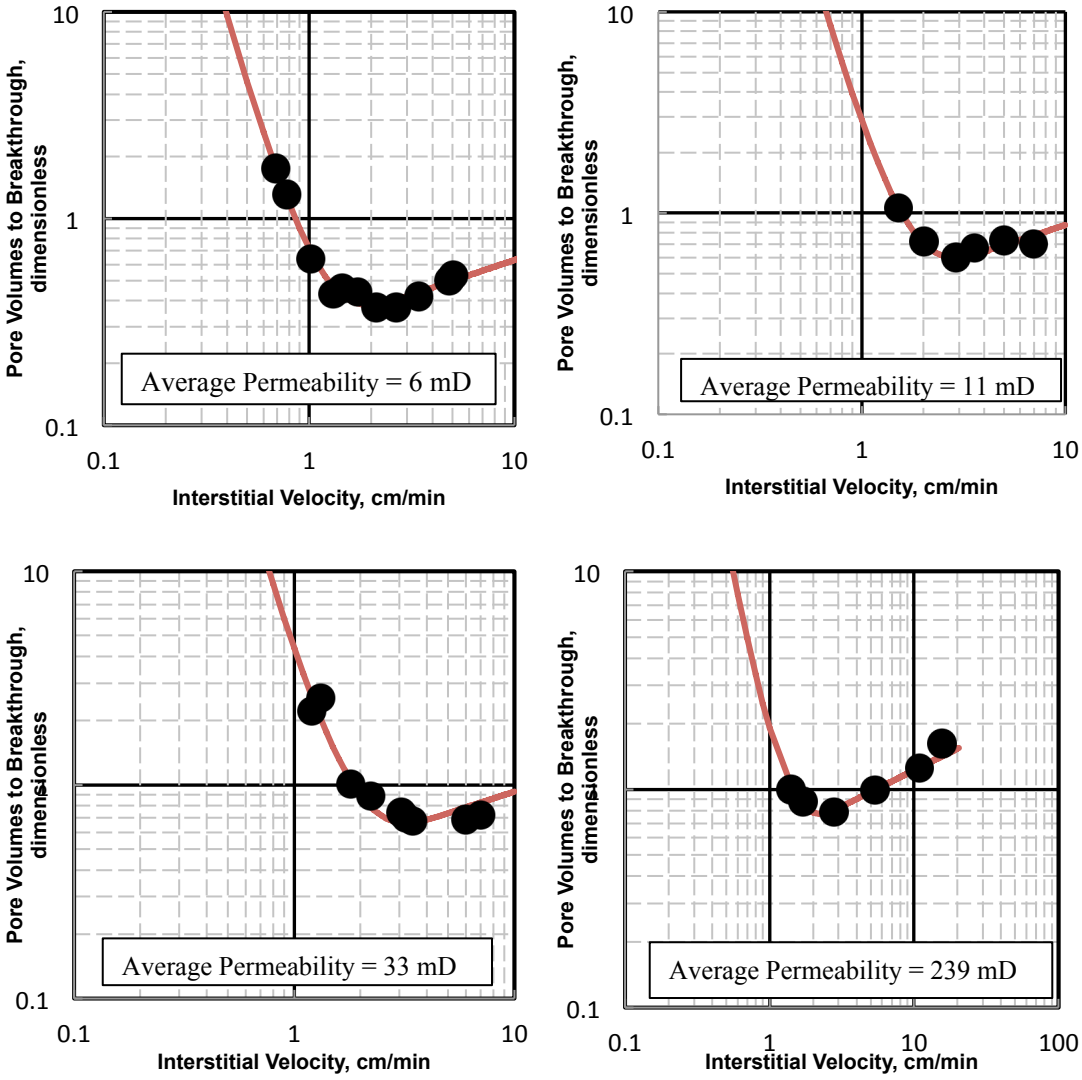

Figure 4.4- Experimental results of wormhole efficiency with different permeabilities.

Fig 4.5 presents the combined results of all four experimental sets. **Table 4.2** summarizes the optimal conditions. The average porosity and permeability values listed are averaged over the set of cores used. The J value listed represents the summation of the square of the differences between the experimental and theoretical values as calculated in Eq. 4.12.

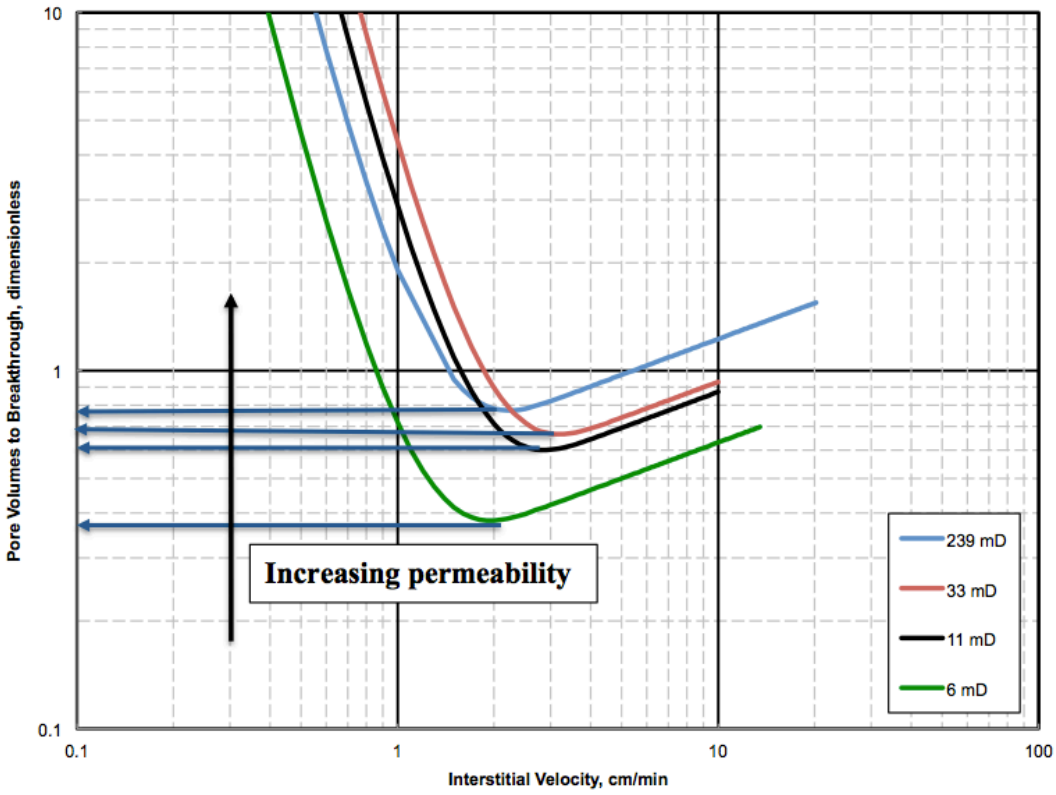

Figure 4.5- Buijse-Glasbergen curve fitted results for different permeabilities.

Table 4.2- Summary of optimal conditions.

Sample	Average Permeability (mD)	Optimum Interstitial Velocity (cm/min)	Optimum Pore Volumes to Breakthrough	J
Indiana Limestone	5.9	1.98	0.376	0.0132
Indiana Limestone	10.7	2.91	0.579	0.0097
Desert Pink Limestone	33.2	3.25	0.64	0.4627
Indiana Limestone	239.3	2.25	0.746	0.0019

The J value, or variance, is very low for all the Indiana limestone samples. This indicates minimal error between the experimental and theoretical values. Indiana limestone is usually used in research due to its homogeneity, resulting in more consistent properties across sets of cores. On the other hand, the Desert Pink limestone samples have a much higher variance. A possible explanation for it involves the greater heterogeneity of this particular rock sample.

Fig. 4.5 shows that as permeability increases, the optimal pore volumes to breakthrough increases. This observation is consistent with the previously published conclusion (Bazin, 2001). The increase of permeability is not proportional to the increase of optimal pore volumes to breakthrough. **Fig. 4.6** plots the optimal pore volumes to breakthrough change as a function of permeability. It is evident that with increasing permeability, $PV_{bt\text{-}opt}$ also increases at a logarithmic rate. The increase rate of optimal pore volumes to breakthrough quickly slows down as the permeability becomes higher, and the effect of permeability on $PV_{bt\text{-}opt}$ becomes negligible.

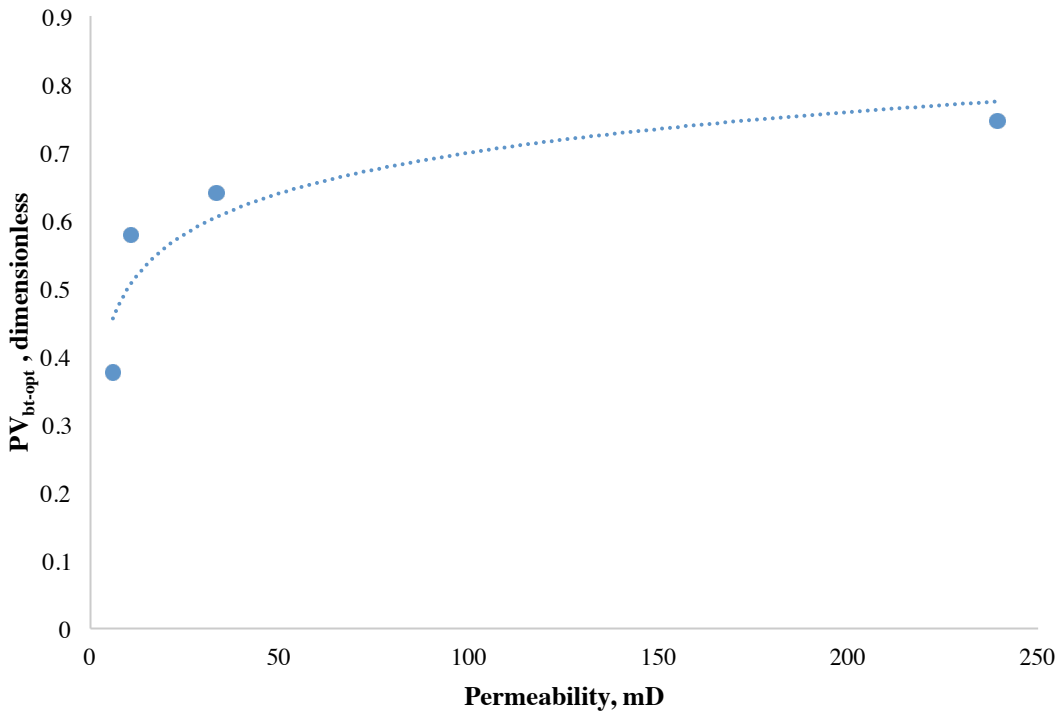

Figure 4.6- Effect of permeability on optimal pore volumes to breakthrough.

Based on the optimum conditions presented in Table 4.2, there is no clear relationship between the optimum interstitial velocity, $v_{i\text{-}opt}$, and permeability. A consistent increasing trend in interstitial velocity exists for the first three low permeability set of experiments. However, the last set of experiment, which contained cores with an average permeability of 239 mD, does not follow this trend. The optimal interstitial velocity decreased from 2.91 cm/min for the 11 mD Indiana limestone samples to 2.25 cm/min for the 239 mD samples. As a result, permeability alone does not appear to capture the mechanism of wormhole efficiency. Previous research has indicated that wormholing in carbonate acidizing is controlled both by operating

conditions and rock properties; injection velocity can be optimized to minimize acid usage, and pore size determines the route of wormhole propagation.

4.4 Pore Structure Effect

Thin section images were studied to investigate the effect of pore structure on the optimal conditions of wormholing. Supposedly, the largest sized pore is directly related to the initiation of a wormhole and wormhole propagation (Wang et al., 1993). An increase in the size of the largest pore helps wormhole propagation. **Fig. 4.7** shows the thin sections for samples from each of the four permeability groups. The figure shows that the sizes of the larger pores for the first three images (Fig. 4.7a, Fig. 4.7b and Fig. 4.7c) are similar in size. However, for the high permeability sample (Fig. 4.7d), the larger pores are much larger.

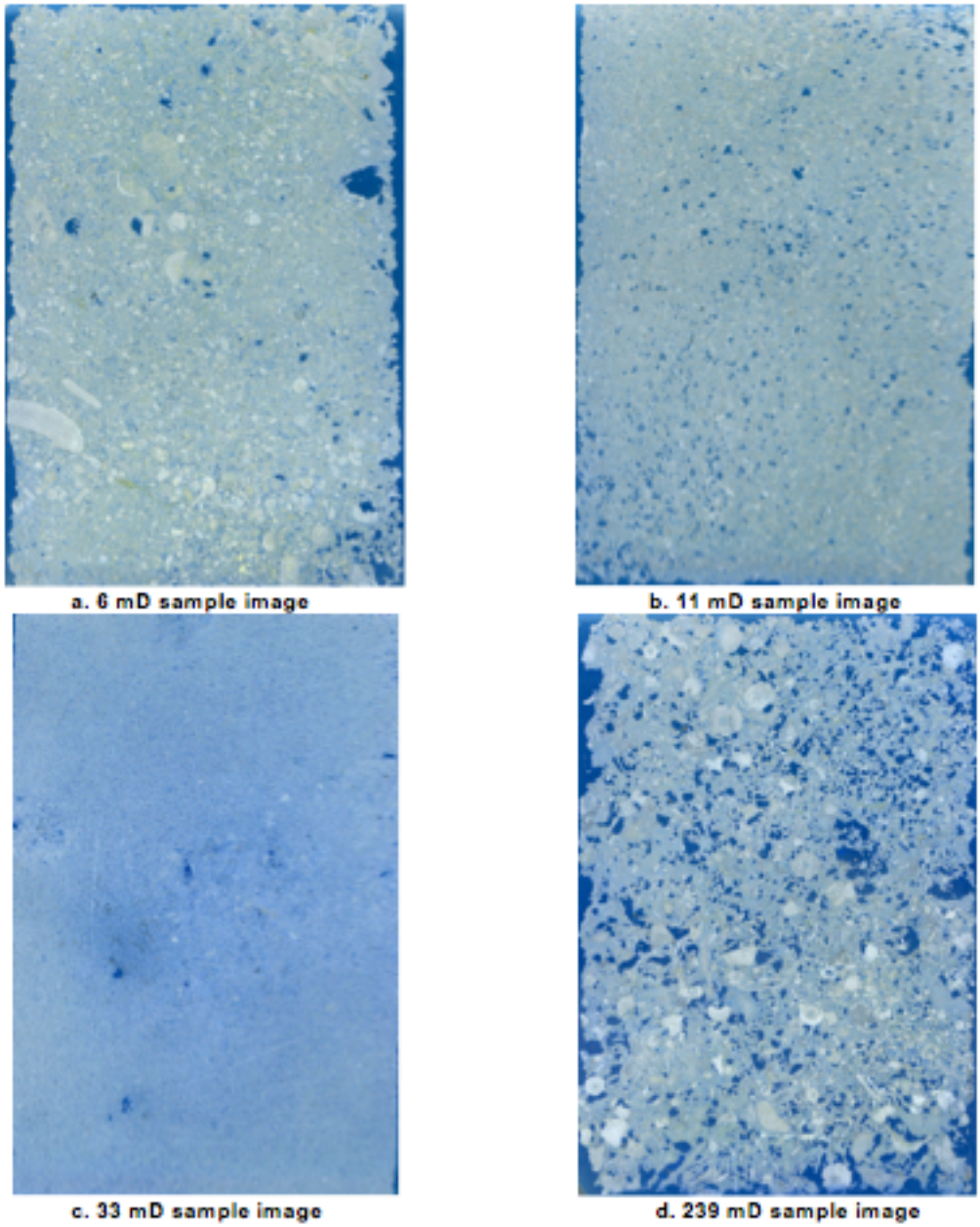

Figure 4.7- Thin section images for each permeability group.

It is also important to note that of the four sets of experiments, set 1, 2 and 4 are Indiana limestone while set 3 is a Desert Pink limestone. The pore structures of the two

different limestone rocks vary greatly (Fig. 4.7). The Desert Pink sample has a higher average porosity than the Indiana limestone (Table 3.2). The porosity of the Desert Pink limestone is primarily in dispersed small pores, which could be the reason for higher optimal interstitial velocity.

Two important observations are made when examining just the Indiana limestone samples (Fig. 4.7a, Fig. 4.7b and Fig. 4.7d). First, as permeability increases, more pores are observed in the thin section (indicating a positive correlation between permeability and porosity). Another observation is that the sizes of the pores do not follow the same trend as permeability. When permeability increases from 6 mD to 11 mD, more pores are distributed over the thin section but the size of the pores do not increase. For the 239 mD high permeability sample, a larger distribution of pores is present in the thin section, and the size of the pores increases as well. This indicates that even though permeability is important in wormhole efficiency, pore structure is also critical for wormhole propagation. Additional research needs to be done to determine the effect of pore structure in more detail.

Ziauddin and Bize (2007) pointed out that pore scale heterogeneities have a major impact on carbonate acidizing treatment. Through several different experiments, they classified carbonates into Reservoir Rock Type (RRT) groups. Compared with their study, the Desert Pink limestone used in this work has a pore structure most similar to the Austin chalk sample (**Fig. 4.8**).

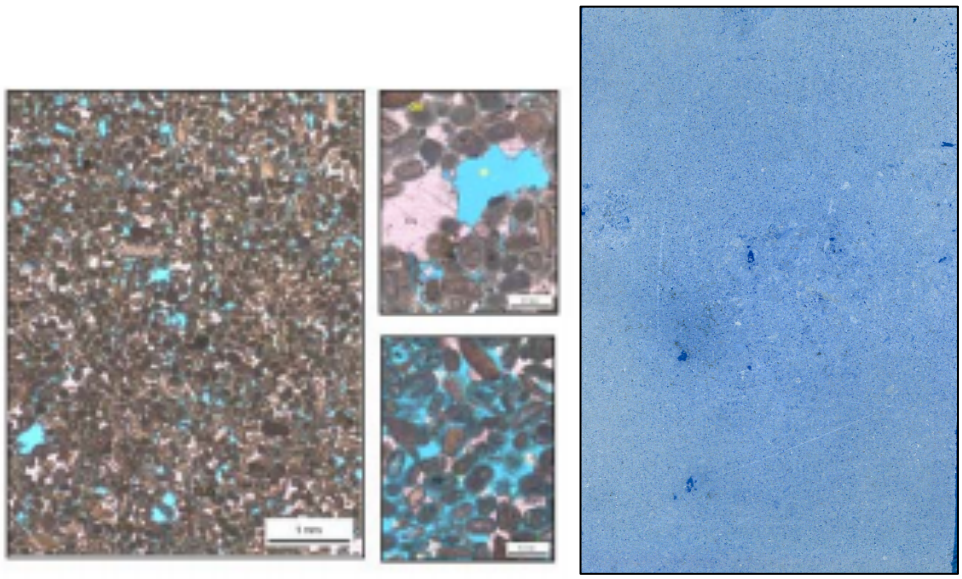

(a) (b)

Figure 4.8- Comparison of (a) Austin chalk (Ziauddin and Bize, 2007) and (b) Desert Pink limestone.

Ziauddin and Bize (2007) classified Austin chalk into a different RRT than Indiana limestone. Indiana limestone was considered to be a "consolidated granular limestone in which dominant porosity is interparticle and is well connected." On the other hand, Austin chalk was assigned to a RRT for "chalky micro granular limestones with both inter and intra particle porosity." Each of the RRTs they defined exhibited similar wormhole efficiency relationships. While many other tests were performed to assign carbonates to RRTs, this observation suggests that the coreflood results for the Desert Pink samples cannot be directly compared to the Indiana limestone samples.

Furthermore, Ziauddin and Bize (2007) observed that the Indiana limestone and Austin chalk groups have similar wormhole efficiency curves but different dissolution

patterns at a given injection rate. CT scanner images of the cores used in this work show a similar observation between the Desert Pink limestone and Indiana limestone. As shown in **Fig. 4.9**, the Indiana limestone exhibits a lot of smaller wormhole branching while the Desert Pink limestone exhibits fewer but more defined branches at comparable acid injection rates. This provides further evidence that Desert Pink limestone and Indiana limestone cannot be compared due to their varied rock properties. CT scanner images for the majority of cores used in this work can be found in Appendix C.

Injection Rate (ml/min)	Desert Pink Limestone	Indiana Limestone (239 mD)
20	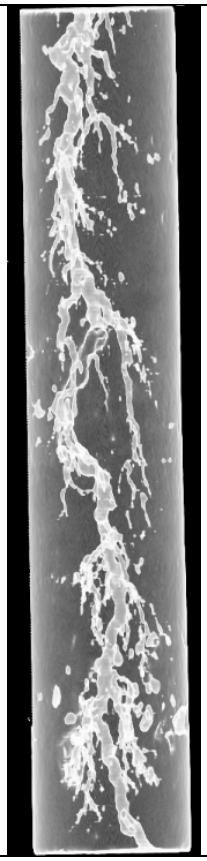	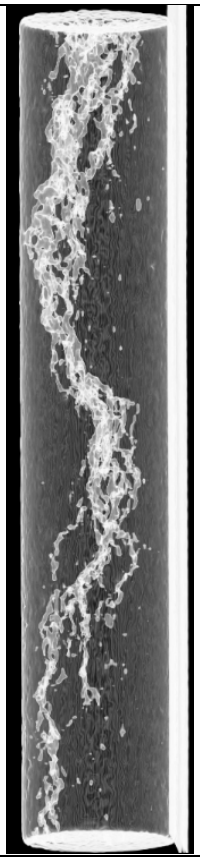

Figure 4.9- Post-acidization CT images of cores from different rock groups.

Zakaria et al. (2015) provided further proof that Indiana limestone and Desert Pink limestone are not comparable based on pore structure. **Fig. 4.10** shows the pore throat-size distribution results they obtained from high-pressure mercury injection tests for an Indiana limestone (with a permeability between 60-65 mD) and a Desert Pink limestone (with a permeability between 75-82 mD). From their results, it is evident that the Desert Pink limestone has much smaller pores.

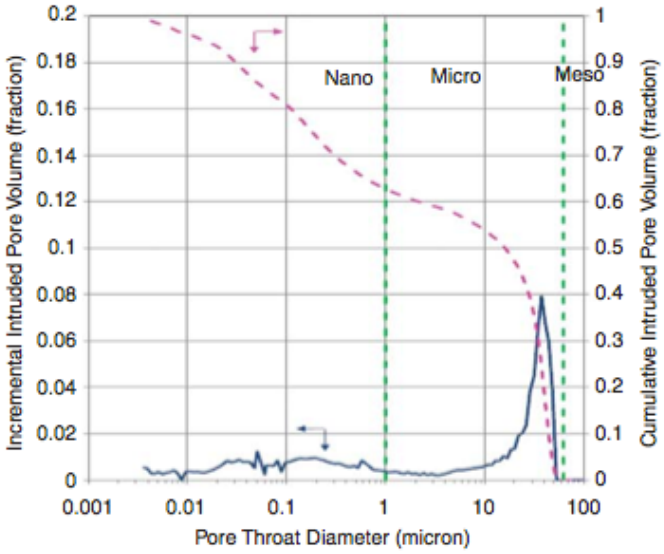

(a) Indiana limestone

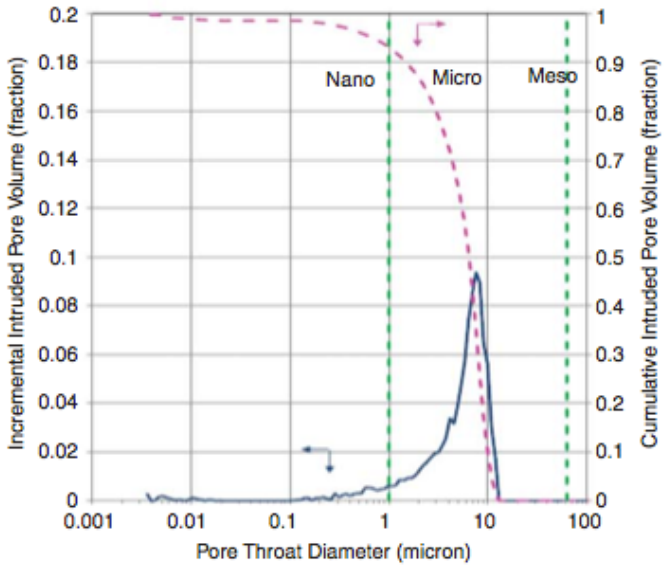

(b) Desert Pink limestone

Figure 4.10- Pore throat-size distribution for (a) Indiana limestone and (b) Desert Pink limestone (Zakaria et al., 2015).

Furthermore, Zakaria et al. (2015) also determined that the Desert Pink limestone has a different flowing fraction, which represents the available fraction of pore space contributing to fluid flow, than the Indiana limestone sample tested in their experiments. To determine this parameter, tracer experiments were performed by injecting potassium chloride, KCl, into core samples. The concentration of the K^+ ion in core-effluent samples at different pore volumes were measured and a tracer-concentration profile was generated for each sample. The flowing fraction was then determined as the cumulative volume that corresponds to the normalized tracer concentration. **Table 4.3** presents the flowing fractions obtained for the samples of interest.

Table 4.3- Flowing fractions for Indiana limestone and Desert Pink limestone (Zakaria et al., 2015).

Sample	Flowing Fraction
Indiana limestone	1.00
Desert Pink limestone	0.75

Zakaria et al. (2015) compared the flowing fraction results with results from coreflood acidization experiments and discovered that samples with lower flowing fractions (such as the Desert Pink limestone) had a lower wormhole efficiency curve (and therefore lower optimum pore volumes to breakthrough value) and an earlier wormhole breakthrough. This appears to be consistent with the results presented in this

work. The authors stated that at a lower flowing fraction, the acid dissolves less rock. This is due to the rock not being as well connected, which results in a smaller contribution of rock matrix to fluid flow. As a result, there is a preferable fluid flow path. This leads to lower acid consumption and therefore a lower wormhole efficiency curve.

These preliminary results confirm that pore structure (micro scale) has more of an effect on wormhole efficiency than permeability (field scale). **Fig 4.11** plots the wormhole efficiency curves for just the Indiana limestone experiments conducted in this work. Additional pore structure studies need to be performed on these samples to more accurately determine the combined effect of permeability and pore structure on the optimal interstitial velocities.

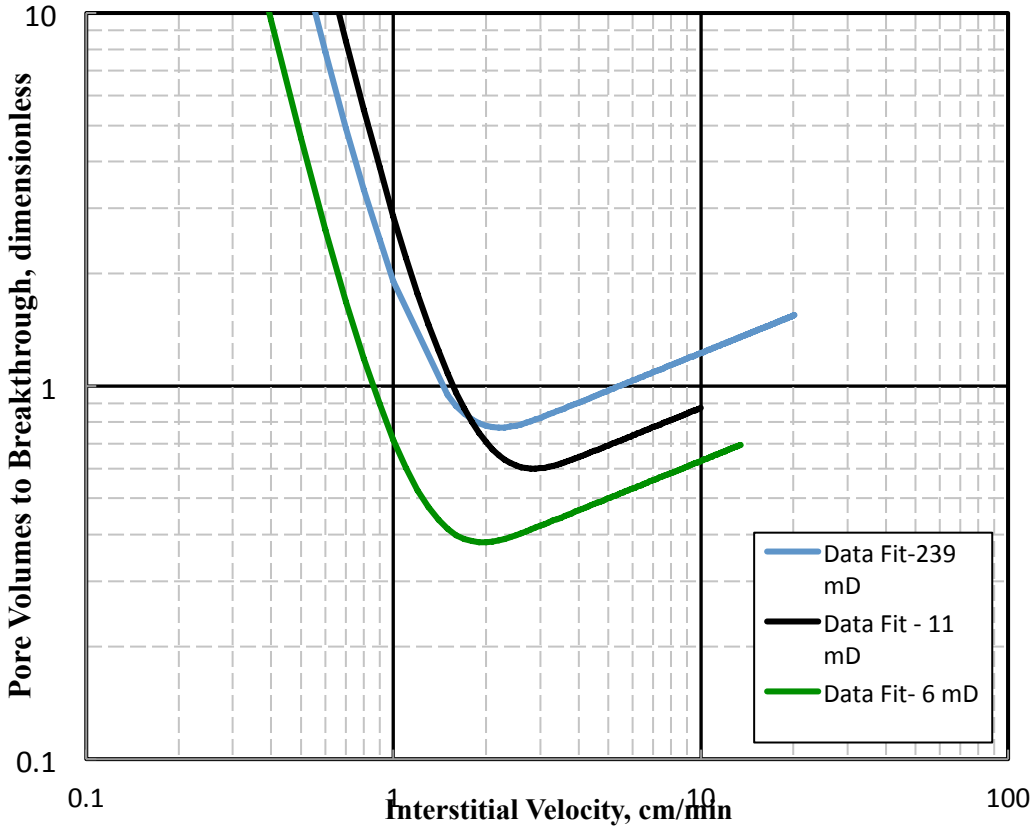

Figure 4.11- Buijse-Glasbergen curve fitted results for Indiana limestone samples of different permeabilities.

5. CONCLUSION AND RECOMMENDATIONS

In this research, four sets of experiments were conducted to observe the effect of permeability on the optimum conditions during carbonate matrix acidizing. Cores with average permeabilities of 6 mD, 11 mD, 33 mD and 249 mD were studied. Based on the permeability experiments, the following conclusions were made:

- The optimum pore volumes to breakthrough value is positively related to the permeability of the samples tested. However, the increase in permeability is not proportional to the increase in pore volumes to breakthrough.
- When the permeability of the rock reaches a certain value, the effect of permeability on the optimum injection condition diminishes.
- Simply using permeability may not capture the nature of wormhole propagation. Pore structure must also be studied.

In addition to the permeability experiments, pore structure was also briefly studied. Based on the thin section images of the cores used during the acidizing experiments, the following conclusions were made.

- The size of the larger pores contributes positively to wormhole efficiency.
- Dispersed small pore distribution yields higher optimum interstitial velocity.
- Optimal interstitial velocity is more controlled by pore structure than just simply permeability.

Based on the results obtained from this research so far, there is a need for further work on permeability and especially pore structure effects on the optimal acidizing conditions. The following studies are recommended.

- Test additional limestones with average permeabilities between 30 mD – 250 mD to determine if trends are consistent across a wider range of data. In particular, determine if there's a permeability threshold where the trend of increasing optimum interstitial velocity with increasing permeability is switched to decreasing optimum interstitial velocity with increasing permeability.
- Explore the effect of pore structure in detail. In particular, focus on the porosity spatial distribution and pore connectivity of the three different permeabilities of Indiana limestones.
- Perform tracer tests on cores of different permeabilities to determine their flowing fractions. See if the results are comparable with the work of Zakaria et al. (2015).
- Develop a model that predicts the optimum interstitial velocity based on a formations rock properties (both permeability and pore structure).

REFERENCES

Abou-Sayed, I. S., Shuchart, C. E., and Gong, M. 2005. Well Stimulation Technology for Thick Carbonate Reservoirs. Presented at the International Petroleum Technology Conference, Doha, Qatar, 21-23 November. IPTC-10647-MS. http://dx.doi.org/10.2523/10647-MS.

Bazin, B. 2001. From Matrix Acidizing to Acid Fracturing: A Laboratory Evaluation of Acid/Rock Interactions. *SPE Production & Facilities* **16** (1): 22-29. SPE-66566-PA. http://dx.doi.org/10.2118/66566-PA.

Buijse, M. A. 1997. Understanding Wormholing Mechanisms Can Improve Acid Treatments in Carbonate Formations. Presented at the SPE European Formation Damage Conference, The Hague, Netherlands, 2-3 June. SPE-38166-MS. http://dx.doi.org/10.2118/38166-MS.

Buijse, M.A. and Glasbergen, G. 2005. A Semiempirical Model to Calculate Wormhole Growth in Carbonate Acidizing. Presented at the SPE Annual Technical Conference and Exhibition, Dallas, Texas, 9-12 October. SPE-96892-MS. http://dx.doi.org/10.2118/96892-MS.

Daccord, G. 1987. Chemical Dissolution of a Porous Medium by a Reactive Fluid. *Physic Review Letters* **58** (5): 479-482. http://dx.doi.org/10.1103/PhysRevLett.58.479.

Daccord, G., Touboul, E., and Lenormand, R. 1989. Carbonate Acidizing: Toward a Quantitative Model of the Wormholing Phenomenon. *SPE Production Engineering* **4** (1): 63-68. SPE-16887-PA. http://dx.doi.org/10.2118/16887-PA.

Dong, K. 2012. *Experimental Investigation For the Effect of the Core Length On the Optimum Acid Flux in Carbonate Acidizing*. MS Thesis, Texas A&M University, College Station, Texas.

Dong, K., Jin, X., Zhu, D., Hill, A.D. 2012. The Effect of Core Dimensions on the Optimum Acid Flux in Carbonate Acidizing. Presented at the SPE Formation Damage Conference, Lafayette, Louisiana, 26-28 February. SPE-168146-MS. http://dx.doi.org/10.2118/168146-MS.

Economides, M.J., Hill, A.D., Ehlig-Economides, C, and Zhu, D. 2013. Petroleum Production Systems, Upper Saddle River, New Jersey: Prentice Hall.

Enerpac. 2015. Instruction Sheet – Hydraulic Hand Pumps.

http://www.enerpac.com/sites/default/files/l1763_i_3.pdf. Downloaded 11 January 2015.

Equilibar Precision Control. 2015. Equilibar back pressure regulator. http://www.equilibar.com/PDF/research-back-pressure-regulators.pdf. Downloaded 09 January 2015.

Fredd, C.N. and Fogler, H.S. 1998. Alternative Stimulation Fluids and Their Impact of Carbonate Acidizing. *SPE Journal* **3** (1): 34-41. SPE 31074-PA. http://dx.doi.org/10.2118/31074-PA.

Fredd, C.N. and Fogler, H.S. 1999. Optimum Conditions for Wormhole Formation in Carbonate Porous Media: Influence of Transport and Reaction. *SPE Journal* **4** (3): 196-205. SPE-56995-PA. http://dx.doi.org/10.2118/56995-PA.

Fredd, C.N. and Miller, M.J. 2000. Validation of Carbonate Matrix Stimulation Models. Presented at the International Symposium on Formation Damage Control, Lafayette, Louisiana, 23-24 February. SPE-58713-MS. http://dx.doi.org/10.2118/58713-MS.

Frick, T., Mostofizadeh, B. and Economides, M. 1994. Analysis of Radial Core Experiments of Hydrochloric Acid Interaction with Limestones. Presented at the International Symposium on Formation Damage Control, Lafayette, Louisiana, 7-10 February. SPE-27402-MS. http://dx.doi.org/10.2118/27402-MS.

Furui, K., Burton, R.C., Burkhead, D.W. et al. 2012. A Comprehensive Model of High-Rate Matrix-Acid Stimulation for Long Horizontal Wells in Carbonate Reservoirs: Part I- Scaling up Core-Level Acid Wormholing to Field Treatments. *SPE Journal* **17** (1): 271-279. SPE-134265-PA. http://dx.doi.org/10.2118/134265-PA.

Glasbergen, G., Kalia, N., and Talbot, M.S. 2009. The Optimum Injection Rate for Wormhole Propagation: Myth or Reality? Presented at the SPE European Formation Damage Conference, Scheveningen, The Netherlands, 27-29 May. SPE-121464-MS. http://dx.doi.org/10.2118/121464-MS.

Golfier, F., Bazin, B., Zarcone, C. et al. 2001. Acidizing Carbonate Reservoirs: Numerical Modeling of Wormhole Propagation and Comparison to Experiments. Presented at the SPE European Formation Damage Conference, The Hague, Netherlands, 21-22 May. SPE-68922-MS. http://dx.doi.org/10.2118/68922-MS.

Grabski, E.R. 2012. *Matrix Acidizing Core Flooding Apparatus: Equipment and Procedure Description*. MS Thesis, Texas A&M University, College Station, Texas.

Hoefner, M.L. and Fogler, H.S. 1988. Pore Evolution and Channel Formation During Flow and Reaction in Porous Media. *AiChE Journal* **34** (1): 45-54. http://dx.doi.org/10.1002/aic.690340107.

Hoefner, M.L. and Fogler, H.S. 1989. Fluid-Velocity and Reaction-Rate Effects During Carbonate Acidizing: Application of Network Model. *SPE Production Engineering* **4** (1): 56-62. SPE-15573-PA. http://dx.doi.org/10.2118/15573-PA.

Huang, T., Zhu, D., and Hill, A.D. 1999. Prediction of Wormhole Population Density in Carbonate Matrix Acidizing. Presented at the SPE European Formation Damage Conference, The Hague, Netherlands, 31 May-1 June. SPE-54723-MS. http://dx.doi.org/10.2118/54723-MS.

Mazel, J.M., Poitrenaud, H. M., and Mbouyou, P.E.M. 2007. Acid Stimulation of Extended Reach Wells: Lessons Learnt From N'Kossa Field. Presented at the SPE European Formation Damage Conference, Scheveningen, The Netherlands, 30 May-1 June. SPE-107760-MS. http://dx.doi.org/10.2118/107760-MS.

McDuff, D., Jackson, S., Shuchart, C. et al. 2010. Understanding Wormholes in Carbonates: Unprecedented Experimental Scale and 3D Visualization. *Journal of Petroleum Technology* **62** (10): 78-81.SPE-129329-JPT. http://dx.doi.org/10.2118/129329-JPT.

Mostofizadeh, B. and Economides, M.J. 1994. Optimum Injection Rate from Radial Acidizing Experiments. Presented at the SPE Annual Technical Conference and Exhibition, New Orleans, Louisiana, 25-28 September. SPE-28547-MS. http://dx.doi.org/10.2118/28547-MS.

Panga, M. K. R., Ziauddin, M., Gandikota, R. et al. 2004. A New Model for Predicting Wormhole Structure and Formation in Acid Stimulation of Carbonates. Presented at the International Symposium on Formation Damage Control, Lafayette, Louisiana, 18-20 February. SPE-86517-MS. http://dx.doi.org/10.2118/86517-MS.

Talbot, M.S. and Gdanski, R.D. 2008. Beyond the Damköhler Number: A New Interpretation of Carbonate Wormholing. Presented at the Europec/EAGE Conference and Exhibition, Rome, Italy, 9-12 June. SPE-113042-MS. http://dx.doi.org/10.2118/113042-MS.

Wang, Y., Hill, A.D., and Schechter, R.S. 1993. The Optimum Injection Rate for Matrix Acidizing of Carbonate Formations. Presented at the SPE Annual technical Conference and Exhibition, Houston, Texas. 3-6 October. SPE-26578-MS. http://dx.doi.org/10.2118/26578-MS.

Williams, B.B., Gidley, I.L., and Schechter,R.S. 1979: *Acidizing Fundamentals*, Monograph Series, Richardson, TX: SPE.

Zakaria, A. S., Nasr-El-Din, H. A., and Ziauddin, M. 2015. Predicting the Performance of the Acid-Stimulation Treatments in Carbonate Reservoirs With Nondestructive Tracer Tests. *SPE Journal*. SPE-174084-PA (in press; posted February 2015).

Ziauddin M., and Bize, E. 2007. The Effect of Pore-Scale Heterogeneities on Carbonate Stimulation Treatments. Presented at the SPE Middle East Oil and Gas Show and Conference, Kingdom of Bahrain, 11-14 March. SPE-104627-MS. http://dx.doi.org/10.2118/104627-MS.

APPENDIX A

Tables A.1 – A.3 present the raw experimental data for the three sets of Indiana limestone. The raw experimental data for the set of Desert Pink experiments is found in Section 4.3.

Table A.1- Indiana limestone (6 mD) experimental data.

Core#	Permeability (mD)	Porosity	Acid injection rate (ml/min)	Interstitial Velocity(cm/min)	PV_{bt}
1	4.9	15%	1.30	0.78	1.31
2	6.2	15%	1.20	0.69	1.74
3	5.9	15%	8.00	4.80	0.50
4	5.8	15%	1.80	1.02	0.64
5	5.7	15%	2.30	1.31	0.43
6	5.2	15%	6.00	3.42	0.42
7	7.3	16%	9.00	5.02	0.53
8	5.1	15%	3.60	2.13	0.37
9	7.1	16%	2.60	1.45	0.46
10	5.7	16%	4.70	2.65	0.37
11	5.6	15%	3.00	1.73	0.44
Average	*5.86*	*15%*	-	-	-

Table A.2- Indiana limestone (11 mD) experimental data.

Core#	Permeability (mD)	Porosity	Acid injection rate (ml/min)	Interstitial Velocity (cm/min)	PV_{bt}
1	11.61	12%	5.0	3.59	0.67
2	9.65	12%	4.0	2.91	0.60
3	12.54	11%	2.5	2.02	0.72
4	12.88	10%	1.8	1.51	1.06
5	8.03	11%	6.2	4.99	0.73
6	9.29	12%	9.3	6.99	0.70
Average	*10.7*	*11%*	-	-	-

Table A.3- Indiana limestone (239 mD) experimental data.

Core#	Permeability (mD)	Porosity	Acid injection rate (ml/min)	Interstitial Velocity (cm/min)	PV_{bt}
1	479.73	16%	10.0	5.34	0.99
2	296.31	17%	30.0	15.53	1.63
3	197.54	16%	20.0	10.87	1.26
4	196.83	16%	5.0	2.78	0.79
5	134.05	15%	3.0	1.70	0.88
6	131.02	16%	2.5	1.41	1.00
Average	*239.25*	*16%*	-	-	-

APPENDIX B

A detailed explanation regarding the conversion factors used to obtain Eqs. 3.7, 4.2, and 4.4 are provided as follows. Conversion factors between oilfield and SI units are provided in Economides et al., 2013.

Equation 3.6 is provided in oil field units.

In standard oil field units: $k = \frac{q*L*\mu}{\Delta p*A}$ ……(3.6)

Equation 3.6 can be written in terms of oil field units as follows.

$$mD = \frac{\left(\frac{STB}{day}\right)*(ft)*(cp)}{(psi)*(acre)} \quad \text{……(B.1)}$$

Equation 3.6 can be written in terms of SI units as follows.

$$m^2 = \frac{\left(\frac{m^3}{s}\right)*(m)*(Pa-s)}{(Pa)*(m^2)} \quad \text{……(B.2)}$$

To determine the experimental permeability in millidarcies, the experimental units are first converted to SI units as shown in **Table B.1**.

Table B.1- Conversion factors for Darcy's Law.

Variable	Experimental Unit	SI Unit	Conversion Details	Conversion (Multiply Experimental Unit)
Flow rate	cm^3/min	m^3/s	$\frac{cm^3}{min} * \frac{1\ min}{60\ sec} * \frac{1 \times 10^{-6}\ m^3}{cm^3}$	1.67×10^{-8}
Length	in	m	1 in = 0.254 m	.0254
Viscosity	cp	Pa-s	1 cp = 0.001 Pa-s	0.001
Pressure	psi	Pa	1 Pa = 1.45×10^{-4} psi	6896.6
Area	in^2	m^2	1 in^2 = .000645 m^2	6.45×10^{-4}

The conversion factors presented in Table B.1 are plugged into Equation B.2 to obtain Equation B.3.

$$m^2 = \frac{\left(1.67 \times 10^{-8} \frac{cm^3}{min}\right) * (.0254\ in) * (.001\ cp)}{(6896.6\ psi) * (6.45 \times 10^{-4}\ in^2)} \quad \text{(B.3)}$$

Equation B.3 is reduced to Equation B.4.

$$m^2 = 9.536 \times 10^{-14} \frac{\left(\frac{cm^3}{min}\right) * (in) * (cp)}{(psi) * (in^2)} \quad \text{(B.4)}$$

Permeability is then converted from SI units (m^2) to oil field units (mD). The following conversion is used to convert Equation B.4 to Equation B.5: 1 m^2 = 1.01 x 10^{15} mD.

$$mD = 96.31 \frac{\left(\frac{cm^3}{min}\right)*(in)*(cp)}{(psi)*(in^2)} \quad \text{(B.5)}$$

Changing units to variables in Equation B.5 results in Equation B.6.

$$k = 96.31 \frac{q*L*\mu}{\Delta p*A} \quad \text{(B.6)}$$

Substituting Equation B.7 for area, A, in Equation B.6 results in Equation 3.7.

$$A = \frac{\pi}{4} d^2 \quad \text{(B.7)}$$

Using experimental units: $k = \frac{122.63*q*L*\mu}{\Delta p*d^2}$ (3.7)

To obtain Equation 4.2, Equation B.7 is substituted into Equation 4.1. Inches are then converted to centimeters thru the following conversion: 1 in = 2.54 cm.

To obtain Equation 4.4, the ID (measured in inches) is converted to centimeters.

APPENDIX C

The cores were scanned using a CT scanner to obtain more information regarding the wormhole structures. **Figs. C.1-C.6** presented the images for each set of rocks (except the 6 mD samples as they were run by Dong, 2012) in order of increasing interstitial velocity (or acid injection rate). In all images, the inlet is at the top of the image.

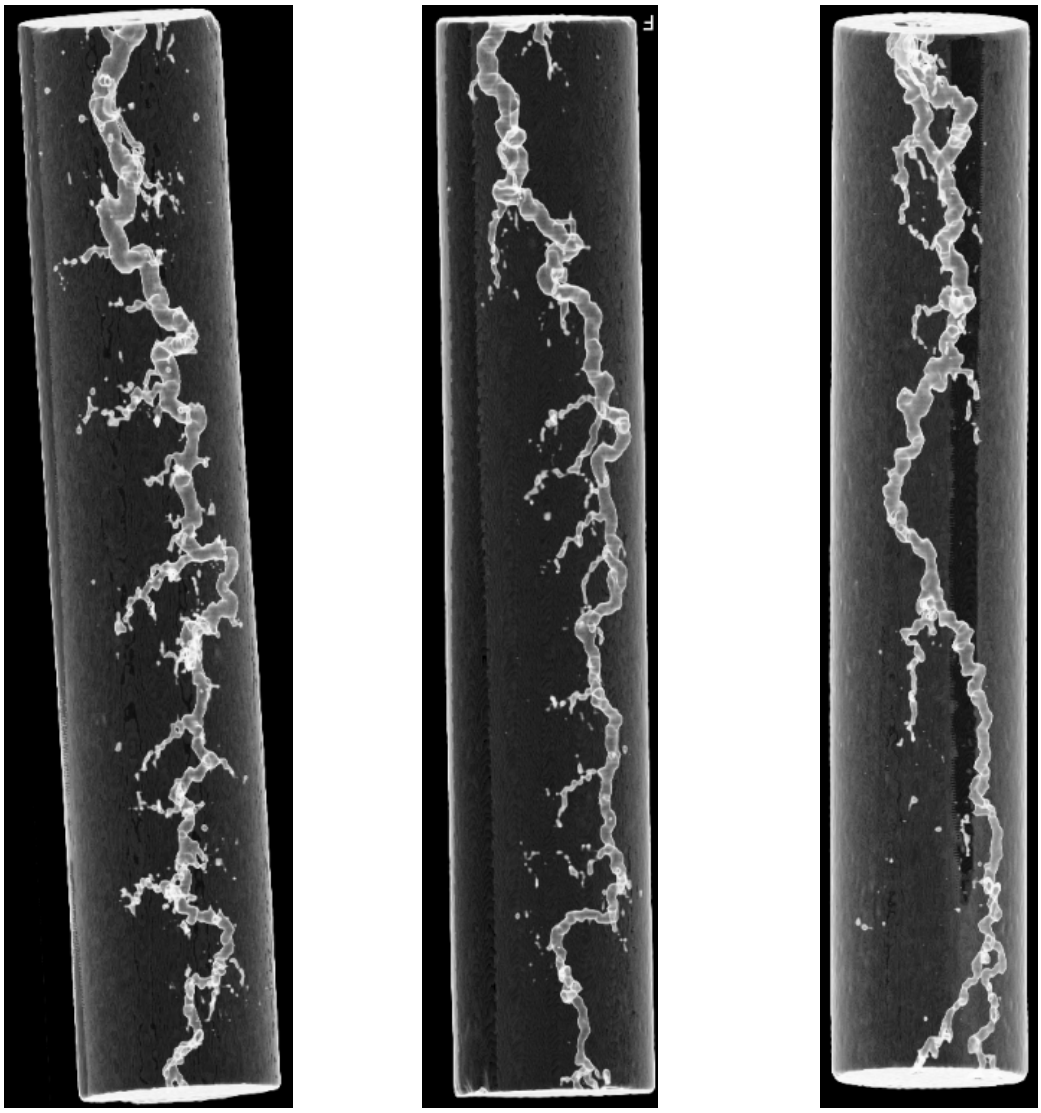

a) Core 4
v_i = 1.51 cm/min

b) Core 3
v_i = 2.02 cm/min

c) Core 2
v_i = 2.91 cm/min

Figure C.1- CT scans of 11 mD Indiana limestone (cores 4, 3 & 2).

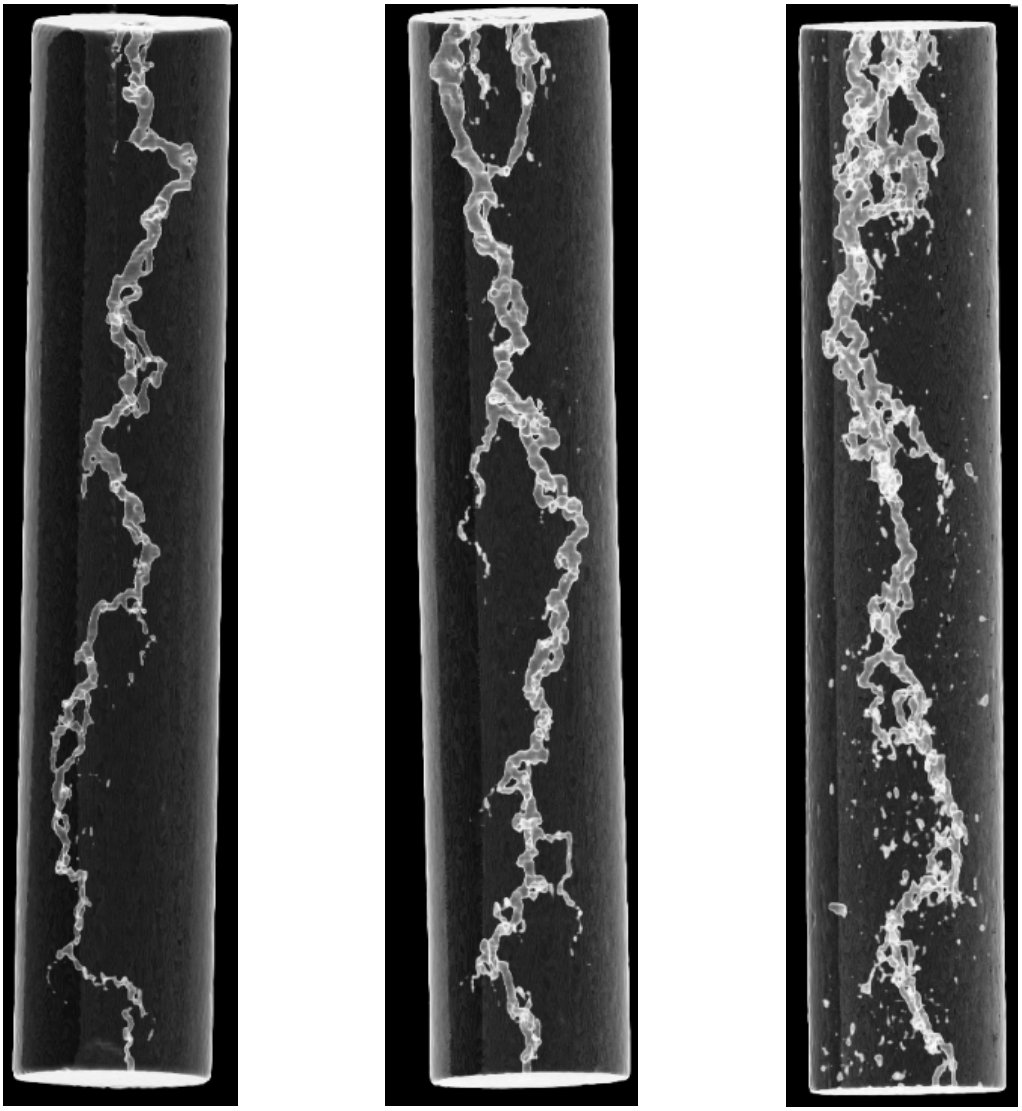

a) Core 1
v_i = 3.59 cm/min

b) Core 5
v_i = 4.99 cm/min

c) Core 6
v_i = 6.99 cm/min

Figure C.2- CT scans of 11 mD Indiana limestone (cores 1, 5 & 6).

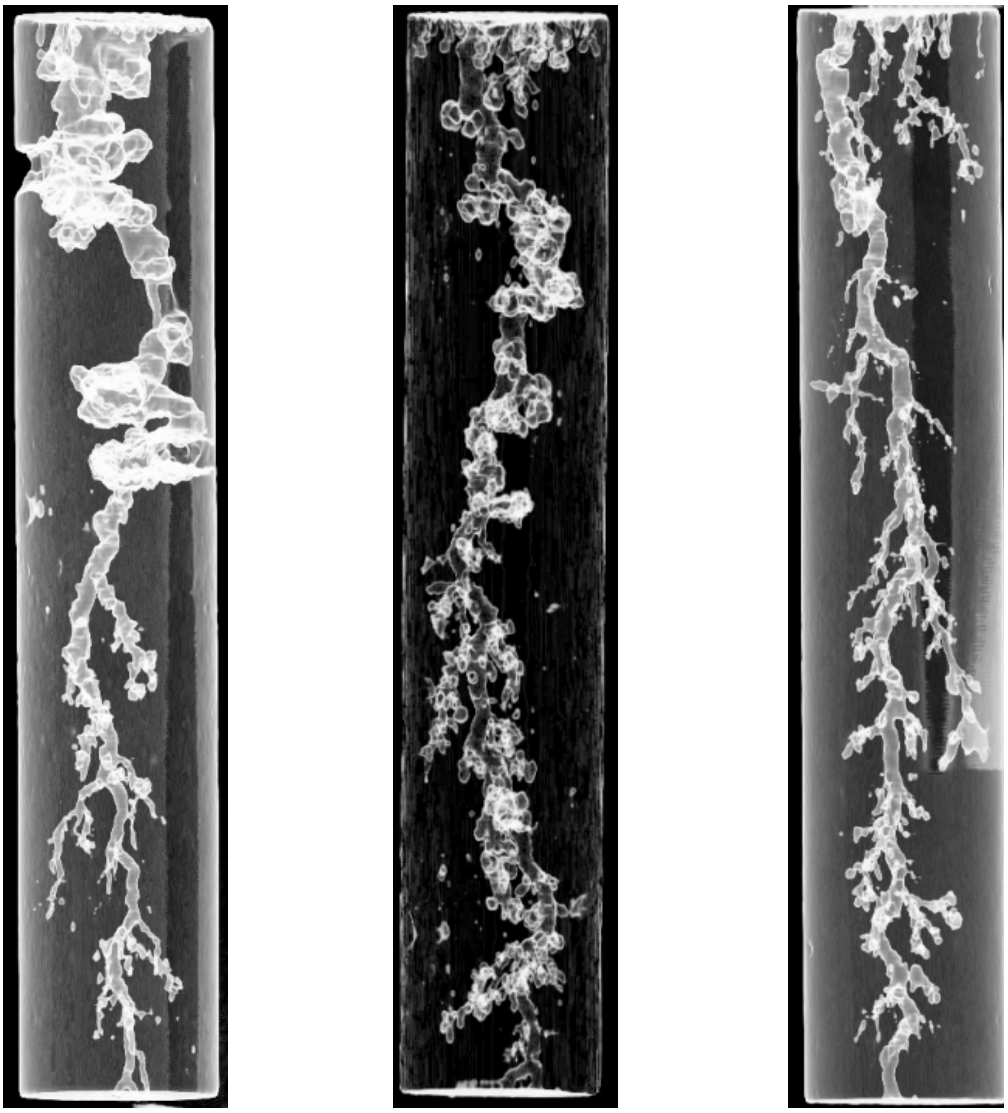

a) Core 6
v_i = 1.32 cm/min

b) Core 9
v_i = 2.22 cm/min

c) Core 5
v_i = 3.06 cm/min

Figure C.3- CT scans of 33 mD Desert Pink limestone (cores 6, 9 & 5).

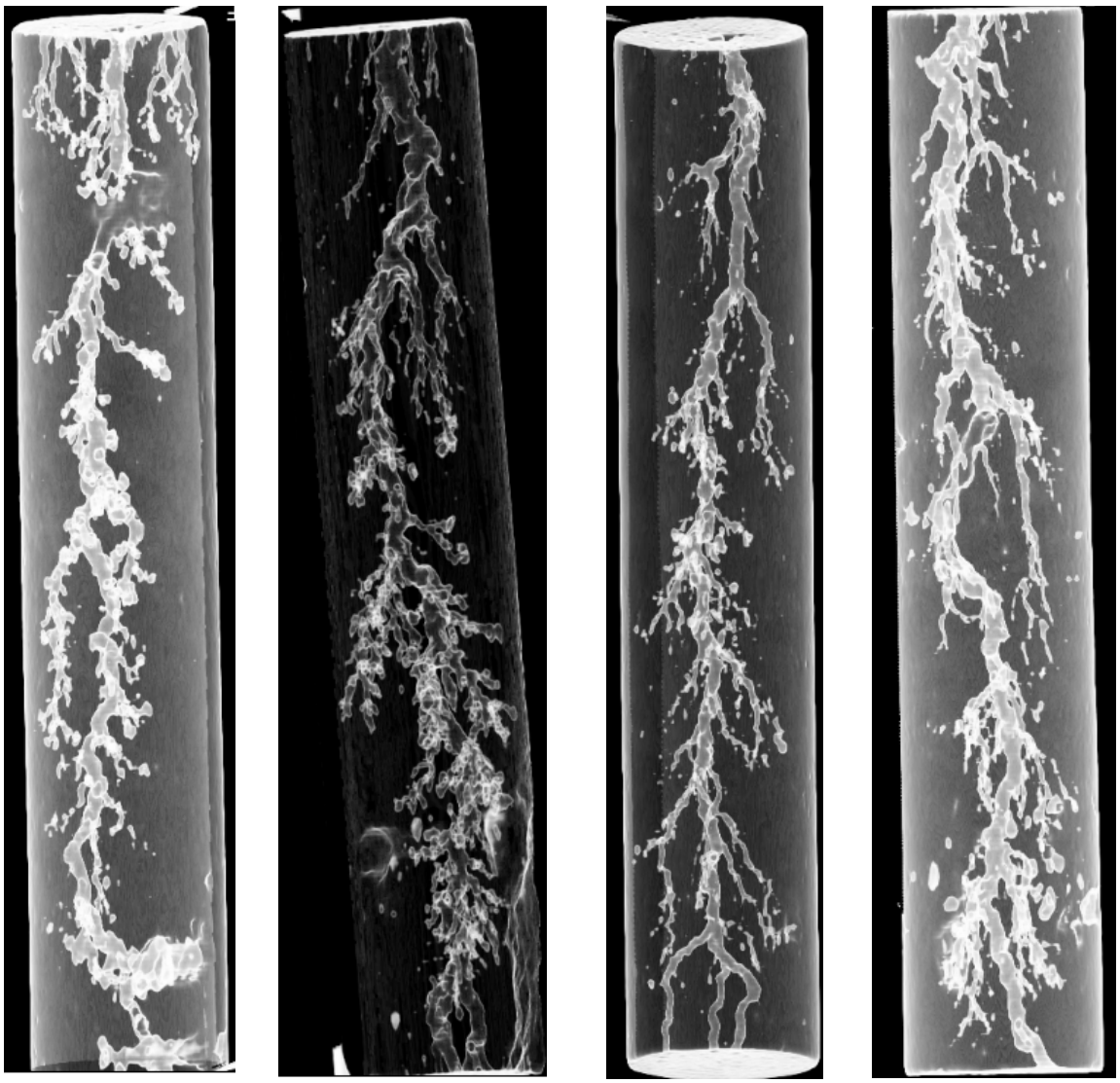

b) Core 3
v_i = 3.20 cm/min

b) Core 1
v_i = 3.46 cm/min

c) Core 4
v_i = 6.01 cm/min

d) Core 8
v_i = 7.03 cm/min

Figure C.4- CT scans of 33 mD Desert Pink limestone (cores 3, 1, 4 & 8).

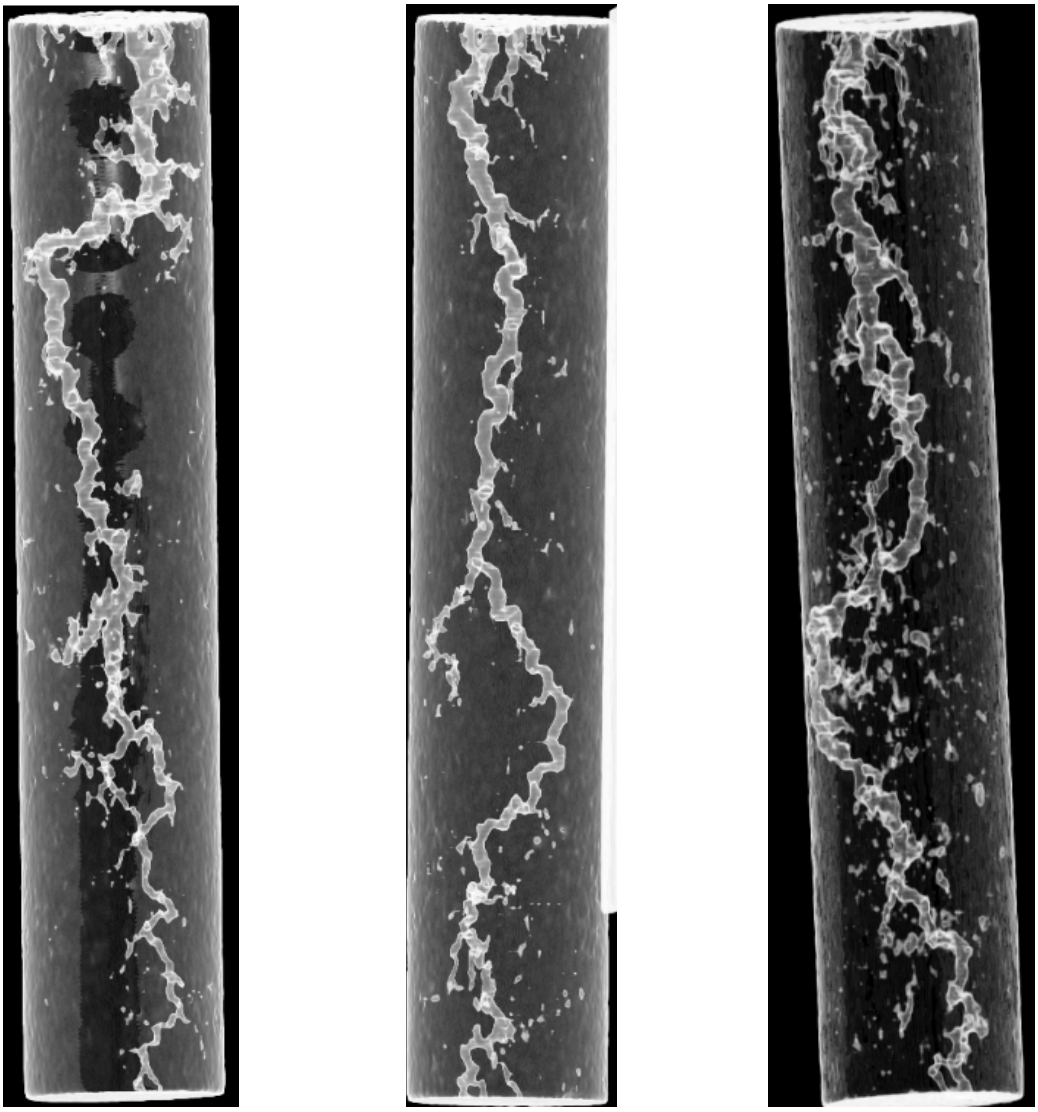

a) Core 6
v_i = 1.41 cm/min

b) Core 5
v_i = 1.70 cm/min

c) Core 4
v_i = 2.78 cm/min

Figure C.5- CT scans of 239 mD Indiana limestone (cores 6, 5 & 4).

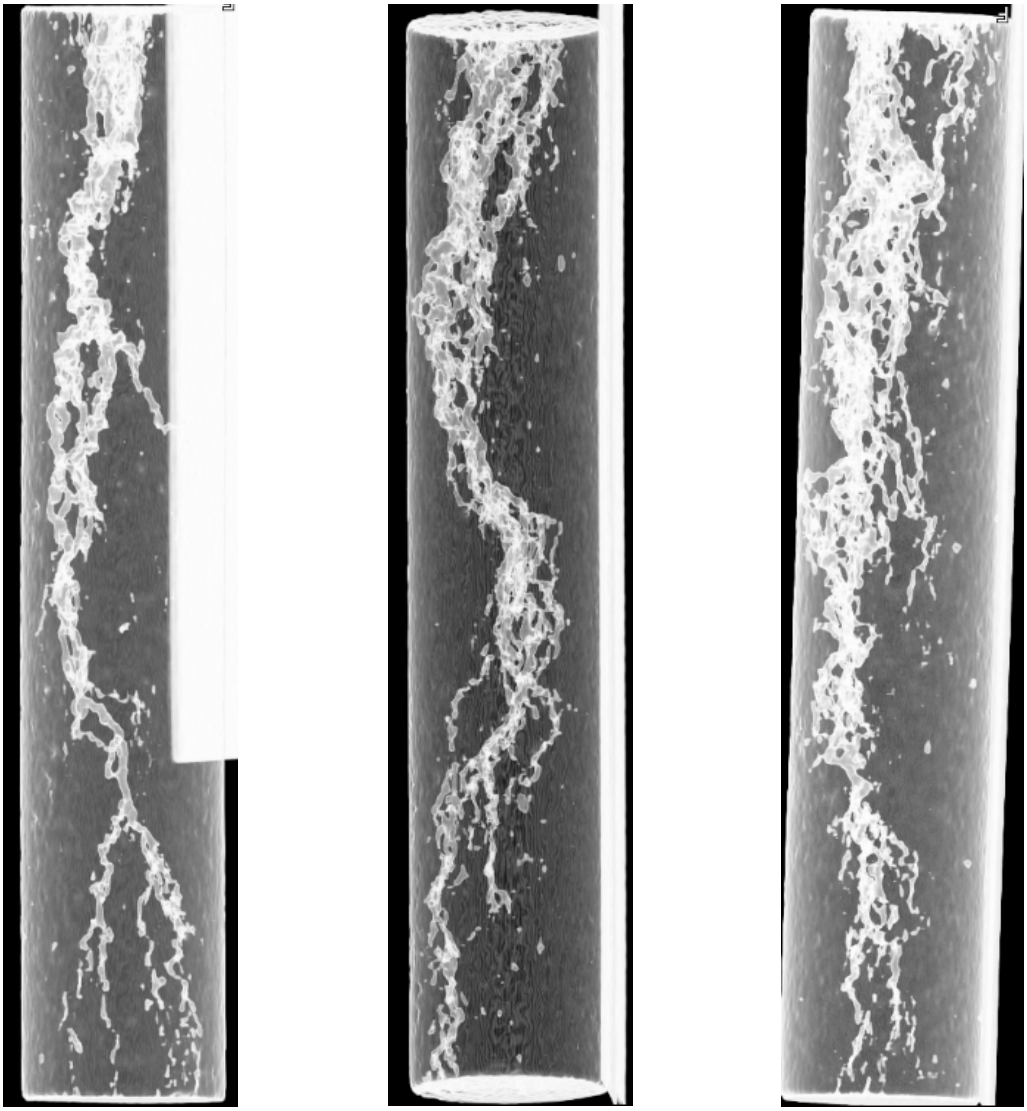

a) Core 1
v_i = 5.34 cm/min

b) Core 3
v_i = 10.87 cm/min

c) Core 2
v_i = 15.53 cm/min

Figure C.6- CT scans of 239 mD Indiana limestone (cores 1, 3 & 2).